Modelling stress-affected chemical reactions in non-linear hyperplastic solids with application to lithiation reaction in honeycomb-structured silicon anodes

Henry Chan Wang Sing

March 2022

Executive summary

This report is concerned with the modelling of stress-affected chemical reactions in the vertices of honeycomb-structured Silicon anodes in Lithium-ion batteries (LiBs), which is inspired by the wall buckling observed in the honeycomb structure as a stress relaxation mechanism. Silicon (Si) exhibits large volumetric expansion during the insertion of Li-ions, in turn generating mechanical stresses, consequently affecting the kinetics of the chemical reaction. The chemical reaction in the vertices is localized at a sharp interface and the kinetics of the interface is modeled based on the chemical affinity tensor concept, which couples mechanical stresses and the chemical reaction rate in a thermodynamically consistent way. The chemo-mechanical problem was formulated for a 2D plate with two reaction fronts that separate the chemically untransformed and transformed phases of Si.

2 finite element procedures for numerical simulations of the reaction front propagation are developed. The first procedure is a linear elastic material model designed to predict the thickness of the chemically transformed layer that induces buckling as well as model the interface kinetics up to the point of buckling. As for the second procedure, an incompressible neo-Hookean hyperelastic model is adopted to describe the equivalent mechanical response of the plate subjected to lithiation in the post buckling regime.

Stability analysis results of the interface were generated from the linear elastic material model and verified with analytical solutions, demonstrating the predictive capability of the present model in small strain approximations. The hyperelastic model predicts the influence of stresses on the interface kinetics depending on the values of the chemical energy parameter. More importantly, it anticipated the retardation of the interface for certain values of the chemical energy parameter in the post-buckling regime which has not been documented previously and could only be achieved beyond the capabilities of analytical techniques.

Table of Contents

Table of figures

List of tables

1. Introduction

The continuous innovation in the current digital world leads to cutting edge electronics being developed across countless industries, ranging from telecommunication to transportation. Ultimately all these devices strongly depend on batteries to supply on-board energy to operate, and Rechargeable lithium-ion (Li) batteries remain the most widely used charge carrier for most electronic device and vehicles, due to its high energy density to weight ratio and low cost [1].

Currently one cannot have a discussion regarding the development of battery technology without mentioning Net Zero. Also known as Climate Zero, in summary means the state where greenhouse gases emitted must be balanced by the ton that is removed from the atmosphere. It is one of the goals that must be fulfilled by 2050 as agreed in the Paris agreement formed in 2015, a legally binding international treaty on climate change adopted by 196 parties at COP 21 in Pairs, with the single goal to limit global warming below 2 degrees Celsius [2]. In the context of decreasing greenhouse gas emissions, the most common way would be to replacing fossil fuel with renewable energy, however since most renewable energy depends on the weather conditions, giant battery plant areas are needed for energy storage to enable stable and on demand energy delivery. The UK has also set specific policies to contribute to the Paris Agreement, one of the ambitious policies include that all new cars and vans should be electric by 2035, and all electric vehicles (EV) require a battery to function [3]. Therefore, these are the reasons are why Battery technology development is extremely critical in solving the net 0 problem which then results in reaching the goals of Paris agreement such that countries around the globe are devoting a lot of resources in research to increase the batteries efficiencies. With Lithium-ion batteries being the most common battery technology to date, intuitively it would be wise to increase its performance and capacity through development of the battery components' material, to accommodate the extra renewable energy generated in the future.

This project is dedicated towards increasing the efficiency and lifespan of Silicon as an anode material in Li-ion batteries (LiBs), by simulating and evaluating its material integrity during the lithiation/de-lithiation cycles. This chapter outlines the difficulties that hinders the progress of Si anode development and background information regarding LiBs will be provided. In addition, the project's key objectives, research methods, timeline and project's justifications will also be presented in this chapter.

1.1. Problem Motivation

Although Silicon (Si) has a high lithium-ion capacity, it suffers from severe mechanical degradation caused by huge expansion and shrinkage from the typical Li-ion extraction/absorption cycle. [4] To overcome this stress induced degradation during the lithiation cycle, the most common method is nanosizing Si. The common to date nano-structuring includes thin films, nanoparticles, porous structures or nanowires, where

each material preparation possess different mechanical stress mitigating mechanism to produce a more stable electrochemical reaction. Nonetheless, the material's life span remains an issue hence the honeycomb structure has been proposed by the researchers [5], to reduce the possibility of material failure from fatigue during the repeated lithiation/de-lithiation cycles. The observations of the morphological change in the honeycomb structure during lithiation demonstrates that the structure can undergo striking deformation during the electrochemical process and that geometrical dimension tailoring should improve the structure's cycle life.

Therefore, the deformation of vertices between triple points of the honeycomb structure have been modelled [6], studying the buckling of a plate subjected to a two-phase lithiation by predicting the time and relative thickness of lithiated layer until buckling. Nevertheless, it is of importance to further investigate the kinetics of the reaction front during the post-buckling stage, where can the non-linear buckling analysis can be completed using Finite-element approach.

1.2. Background information

1991 marked the commercialization of the Lithium-ion battery developed by a Sony team lead by Mr. Yoshio Nishi, the structure of these high energy density and lightweight LiBs are displayed on figure 1 below [7].

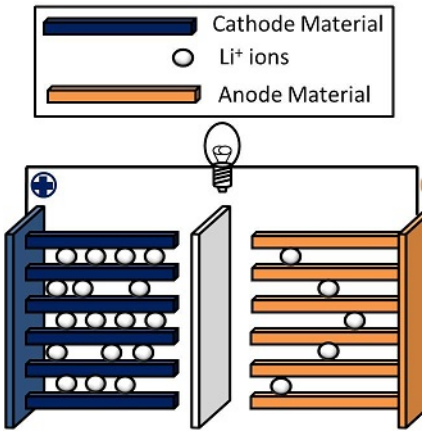

Figure 1: Schematic of a Lithium-ion battery [8]

1.2.1. Battery structure:

Figure 1 shows that each battery must contain 4 key components: 1. Cathode, 2. Anode, 3. Separator 4. Electrolyte.

1. The cathode is the positive charged plate as well as the source of lithium ions. Since battery generates electricity through chemical reactions with lithium ions, the battery cannot function without it. Lithium itself is extremely unstable since it always wants to lose the only 1 electron on

its outer shell, hence usually the lithium is combined with a metal oxide, also known as the "active material", to make up the cathode.

2. The anode is the negatively charged plate and is coated with an active material as well but unlike the cathode, this active material's function is to act as a storage. The anode has 2 main functions: Allowing electrical current to flow into external circuits and absorbing or emitting of the Li-ions that were transferred from the cathode.
3. The separator acts as the barrier/gate between the cathode and the anode, which not only stops the electrons from direct flow and short circuiting, it also increases the safety of the battery by acting as an insurance layer, in case the electrolyte dries up, only allowing Li-ions to pass through.
4. The electrolyte is similar to the separator however it serves as a medium for transporting only Li-ions from cathode to anode through the separator during charging, one may also think of it as a filter. Usually composed of salt dissolved in organic solvent.

1.2.2. Process of electricity generation:

During a Charge cycle, the power source will attract and remove the electrons from the Li-ions and travel through the external circuit as shown in figure 1, reaching the anode. As the positively charged ions are attracted to the negatively charged terminal, they reach the anode by flowing through the electrolyte and micro-permeable separator, resulting in the storage of lithium ions and electrons on the anode side. During a Discharge cycle, Since Lithium would always want to migrate back to their stable state which is being part of the metal oxide, they would go through the electrolyte and separator again. Due to this tendency the electrons move through the external circuit to reunite with the lithium ion in the cathode, therefore generating an electrical current.

During the process of where electrons and Li-ions reunite at the electrodes through intercalation, an electronically insulating and ionically conducting passivation layer is formed between the electrolyte and the electrode known as the solid electrolyte interphase (SEI). The buildup of the SEI layer consumes active Li and electrolyte material, causing the cell to lose capacity as well as increased battery resistance. [8] Nonetheless, SEI is considered a blessing in disguise, due the fact it prevents any direct contact between electrons and the electrolyte, saving the electrolyte from degradation. Thus, a dense and optimized SEI is crucial for the electrochemical stability of the battery.

The materials composition of the battery components can vary with each presenting different advantages in charging speeds and safety but in this report, we will only focus on the anode material. Currently, the most used anode material for Li-ion batteries is still graphite. Originally, the graphite's intercalation electrode structural stability and low electrochemical reactivity was the most suitable candidate as an anode.

Even though it has demonstrated consistent performance, its energy capacity is unable to catch up to the ongoing electrification of the modern world.

Elements	Si	Sn	Al	Ge
Density (g/cm^3)	2.3	5.8	2.7	5.3
Conductivity (S/m)	1×10^3	9.1×10^6	3.8×10^7	2×10^3
Gravimetric Capacity (mAh/g)	4200	959	993	1600
Volumetric Capacity (mAh/cm^3)	9782	7063	2681	8526
Average potential (V)	0.40	0.50	0.38	0.60

Table 1: Specification of Li alloyable metals [10]

In order to capitalize on a better anode solution, materials based on electrochemical alloying was explored, specifically the ability to electrochemically alloy with Lithium. Table 1 shows a few prospective elements that contains this characteristic, along with their theoretical capacities and potentials. These include Silicon (Si), Tin (Sn), Aluminum (Al) and Germanium (Ge). Conventional graphite anode material possesses a specific capacity (aka gravimetric capacity) of 372 mAh/g, and a volumetric density of 841 mAh/cm3. [9] Clearly, Silicon has the highest theoretical gravimetric capacity of 4200 mAh/g which is more than 10 times that of graphite and approximately 4 times of Aluminum and tin. Germanium comes in second due to its high density compared to Silicon. Nonetheless, the next most promising candidate for the anode active material would be the Earth's 2nd most abundant element – Silicon. Not only due to its availability and low cost, moreover it's specific capacity above shows that its energy density is a lot higher compared to any other elements as well as being light, making it the ideal anode material for batteries.

However, taking in such large amount of lithium involves a volatile volumetric change up to 400% during the lithiation process giving rise to mechanical stresses within Si, which in turn can cause significant deformation and pulverization of the electrode, resulting in severe capacity fade over time. [10] Therefore, a lot of factors need to be investigated in order to solve this problem so that Si can be successfully implemented into every Li-ion battery. These solutions will be further mentioned in Chapter 2.

1.3. Project Specification:

Only through understanding the ongoing deformation behavior of the honeycomb structure, can one predict then establish geometric optimization to increase Si anode's life cycle. The aim of this report is to investigate and model the chemical reaction of the Si Anode prepared in a honeycomb micro-architecture, in the presence of mechanical stress during lithiation. This is done by performing systematic analysis on the vertices of the structure using finite element methods as well as developing a computer simulation of the micro-architecture undergoing the electrochemical reaction. The inclusion of modelling the post buckling behavior of the vertices is another step to further increase the accuracy of the predications on the

deformation. During, simulations factors that may affect the reaction front kinetics such as chemical energy parameters and geometry of the vertices are evaluated through testing. Key objectives for the investigation:

- Element formulation: Development and gathering of constitutive equations that models the behavior of lithiated and un-lithiated material in the vertices of the Si Honeycomb structure during lithiation.
- Code a script that can model the mechanical deformation of the Si structure's vertices caused by this electrochemical process. During the computer simulation, the program should demonstrate the followings:
    - Structure being subjected to lithiation (Propagating reaction front)
    - Loss of internal stability, buckling
    - Behavior of the structure Post buckling

1.4. Duration of report & Research methodology:

This project is carried out from 1/10/2021 to 17/3/2022. In this report, the available literatures regarding electrochemical processes involved with Si are reviewed in journals and scholarly articles. Knowledge on fundamentals of relevant physics and mathematical operations needed for the modelling process are obtained from textbooks. Hence keeping up to date with cutting-edge research but also identifying opportunities to further continue previously uncompleted investigations. Most modelling are done on personal computer thus there is no risk management needed.

1.5. Project justification:

1.5.1. Educational benefits:

Coding and computer modelling is essential being an engineer in this day and age, since the main objective of this project is to model and simulate the Si structure's chemical and mechanical behavior subjected to lithiation, it is useful in terms of experience on a specific software and self-learning was horned from using an unfamiliar coding language. The project requires a broad understanding of the chemistry as well as continuum solid mechanics, these areas of study are relevant to most engineering disciplines, this project presents the opportunity to apply theory to a practical problem. Furthermore, Finite element method is used across most engineering industries to analyze any given physical phenomenon. Designing an experiment with the constraints considered sharpened problem-solving skills and project management which are key attributes in any engineering operation.

1.5.2. Societal benefits:

The increasing dependency in renewable energy to solve the severe global warming effects caused by burning fossil fuels means more energy storage plants are needed. Through researching battery technology,

looking into its component to make small enhancement can create large improvements in storage efficiency, reinforcing the reliability of renewable energy for on demand power supply. EVs also depend on battery capacity greatly, better battery technology will also boost efficiency and quality of life as the vehicles are able to deliver greater performance than previous attempts. Since this report is dedicated in enhancing Si's anode life-cycle stability, this research may encourage increased adoption of Si as an anode material which in turn means more efficient energy storage, the effect may very well resonate around the globe given how much cheaper Si is compared to other anode materials, meaning it is extremely easy to obtain such material.

2. Literature Review:

2.1. Electromechanical mechanism of Silicon:

2.1.1. Lithiation

It is important to determine lithiation dynamics and stress evolution in Si particles during lithiation precisely before moving forward to improve current nano-structured solutions. Crystalline Silicon (c-Si) and amorphous Silicon (a-Si)'s reactions to lithiation were studied in [11] to better understand the Li-Si reaction, their situ transmission electron microscopy (TEM) results show unexpected differences in terms of fracture behavior and kinetics of the lithiation during the solid-state reaction for the c-Si and a-Si sphere cases.

When a-Si spheres of 562nm were subjected to lithiation, there was on average 204% volume expansion. On the basis of electrochemical results, previous work assumed that lithiation of a-Si is always a diffusion-controlled single-phase process where an Si-Li solid is formed evenly throughout the structure, but current TEM results show sharp change in Li concentration between Si-rich core and lithiated outer shell, showing a steep concentration gradient. This is similar to the c-Si which also have a two-phase reaction to form highly lithiated amorphous LiSi.

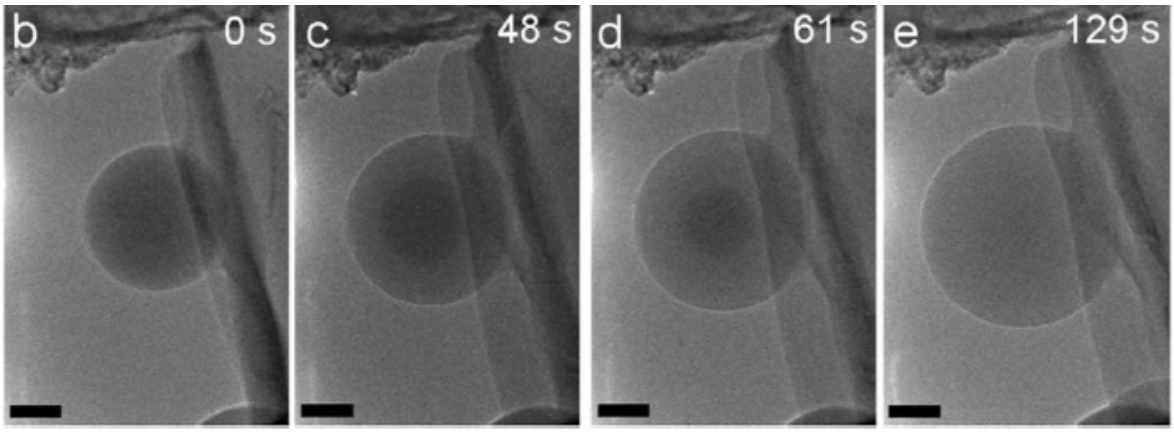

Figure 2: Time series of the lithiation of a single a-Si sphere [12]

Figure 2 concludes that the lithiation process is controlled by a kinetic barrier (reaction front) breaking Si-Si bonds. Rate of Si-Si bond breakage is faster when higher concentration of Li is near the SI-Si bond, as

they weaken the bonds. This also explains why a highly lithiated amorphous phase forms as the c-Si is consumed near the reaction front. Their data shows similar trait for a-Si, thus implying that lithiation is not just a diffusive process but involves Si-Si bond breakage in the amorphous phase. The rate of breaking Si-Si bonds is probably slower than the diffusion of Li in LiSi phase, explaining the distinct interface observed between the two phases. [12]

LiSi thicknesses of sphere subjected to Chemical lithiation (where spheres are directly in contact with lithium metal) and electrochemical lithiation were approximated as a function of time in [14]. Results show chemical lithiation reached maximum LiSi thickness much faster than electrochemical reaction, again demonstrating that reaction kinetics at Si-rich core being concentration dependent as discussed above. More importantly, in both cases lithiated thickness increases linearly with time, suggesting controlled by short-range interactions at an interface instead of by diffusion.

2.1.2. Amorphous vs Crystalline Silicon:

Key differences between a-Si and c-Si lithiation is that Fracture has shown to occur on c-Si spheres larger than 150nm in diameter but not on a-Si spheres (even with diameters of 870nm). [13] In c-Si particles, tensile hoop stress develops at the surface due to two-phase lithiation process, where newly created Li_xSi at the reaction front pushes out previously formed Li_xSi leading to tension on the surface. Moreover, due to the crystallography of the c-Si, it is anisotropic in nature, leading to stress intensification and fracture at specific locations compared to the isotropic nature in a-Si, thus meaning c-Si is more prone to fracture. Other than that, concentration of Li in the Li_xSi phase form in a-Si is less than in c-Si, meaning there is less significant volume expansion at the interface hence lower stresses. Second reason for less stress in a-Si is that kinetics of the bond-breaking in a-Si is a lot quicker than the kinetics of diffusion in Li_xSi, unlike in c-S. Quicker rate causes larger Li concentration gradient in a-Si due to Si bond breaking keeping up with the diffusion rate whereas there is little to no concentration gradient of c-Si as the Si bond breaking is not quicker than the diffusion process. Meaning overall c-Si has a larger fracture size with a similar reaction mechanism due to a-Si having less tension at the surface.

Another difference between the 2 cases is that c-Si's interface velocity was reported to slow dramatically with increasing lithiated-layer (Li_xSi) thickness while a-Si doesn't. Most likely due hydrostatic pressure that evolves near the interface, altering the diffusion in the vicinity of the reaction front. However, there is no slowing in reaction front propagation observed in a-Si, this suggests lower magnitude of hydrostatic stress compared to c-Si, showing consistency with previous fracture behavior comparisons. [14]

2.1.3. De-lithiation & Subsequent-lithiations:

Most a-Si spheres remain amorphous after lithiation. As mentioned above, during the first lithiation cycle, concentration boundary was evident, on the contrary de-lithiation seems to be a single-phase mechanism with no concentration boundary visible, which is consistent with previous assumptions as Si-Si bond breaking doesn't occur during de-lithiation. Additionally, it is worth noting the development of hoop tension at the surface during de-lithiation due to lower li concentration, but the stress is not significant enough to cause fracture.

Subsequent lithiations are different to the 1st as no concentration boundary is visible also implying a single-phase diffusion process and that there is a change in a-Si's material properties compared to the initial lithiation cycle. Possibly due to trapped Li in the a-Si matrix after first de-lithiation material, which was proven by de-lithiated a-Si particles being 25% larger than the initial particle volume, suggesting that Li remained in the sphere was of lower density. Another reason for change in reaction mechanism is the structural transition of a-Si after the first lithiation, causing extra Si dangling bonds (an unsatisfied valence on an immobilized atom) in a-Si hence no bond-breaking process is involved. [15]

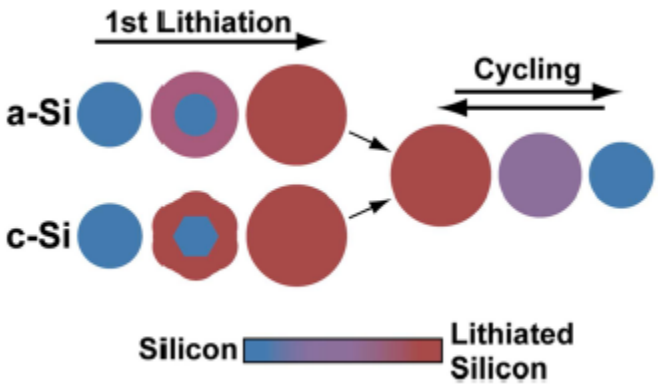

Figure 3: Summary of the first lithiation and subsequent cycling of a-Si and c-Si. Color-coded by Li content with blue as pure Si and red as the fully lithiated phase. [12]

2.1.4. Overall lithiation cycle:

A two-phase lithiation mechanism for a-Si is identified which is important for this investigation as stress evolution and fracture behavior is strongly correlated with the lithiation mechanism. It was shown that a-Si undergo a much more management physical transformation than c-Si during the first cycle and is more desirable as an active anode material. During first lithiation, critical size for fracture is larger for a-Si and lithiation reaction front velocity doesn't slow down in a-Si compared to c-Si, which explains the difference in stress evolution between 2 cases.

2.2. Nanosizing:

Even if Si has extremely high specific capacity, taking such high quantity of Li-ions does comes with a trade off with reduced structural integrity as the material involves a volume expansion up to of 400% during lithiation. Stress induced degradation is generated by these volatile volume changes, which causes cracking and pulverization of the Si anode, decreasing the electrical contact as well as fading capacity in the long run. Therefore, nanosizing the material has been proposed to accommodate the volumetric change and increase the stress resilience of the Si anode.

These are the main nanosizing preparations of Si: Thin film, nano particles, 3D structures or nano wires. The main difference between them is their stress release mechanisms and fabrication method.

Thin film: thin films are commonly produced by chemical vapour deposition onto the current collector and the direct deposition of a metal substrate allows direct conduction pathway for lithiation. Even though think films provide strong electrical contact which favors electrochemical reactions, the storage capacity in planar thin films batteries remains low for viable commercial use. Moreover, it doesn't accommodate large volume expansion across the surface well compared to other nanomaterials. This is Evident as degradation of specific capacity is seen in figure 4, showing the stress-induced breakup of the a-Si thin film with 1um thickness into smaller islands. Large tensile stress placed on the electrode during volume expansion causes cracks to form, exposing fresh silicon edges and the film is separated into silicon island which is visually similar to a dry lakebed. This process then proceeds with these smaller islands piling up, which form pillars and eventually delaminating, causing gradual loss of connectivity between the electrode and the current collector as the lithiation cycles goes on. [16]

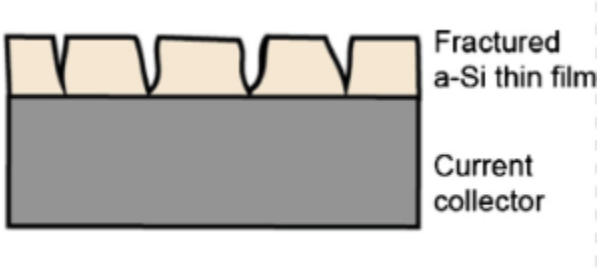

Figure 4: Vertically fractured a-Si thin film anode after 1st electrochemical cycle [17]

Nanoparticles/ Nanoscale powder anodes: pure Si anodes particles/nanoscale powder anodes are dispersed onto an active material matrix mixed with different binders. More specifically, generation of nanocomposites comprising of Si powder coated with thin layer of amorphous carbon serving as an interfacial adhesion layer, then embedded into a more ductile carbon matrix. The carbon coating enhances structural stability and prevents local capacity fading by maintaining consistent electrical contact between Si particles. The key disadvantage is that The Bulk Si anode tend to agglomerate during lithiation cycles,

and the sizes of individual particles increase resulting to poor lithiation kinetics after cycles of large volume expansion. Despite that, it is considered one of the more commercially viable options compared to other nanomaterial preparation due to its scalability. [17]

3D pores: 3D porous Si particles with nm scale wall thickness can handle large strains without cracks of pulverization simultaneously maintaining specific capacity after many electrochemical cycles. Its unique shape and porous structure allow faster transportation of Li-ions through the electrolyte hence providing faster intercalation reaction of Li-ions and sustaining high specific capacity even at high charging currents, agreeing with literature on the overall lithiation process, where chemical reaction rate is kept up with diffusion rate, leading to a steep Li concentration gradient hence exerting less stress overall on the structure.

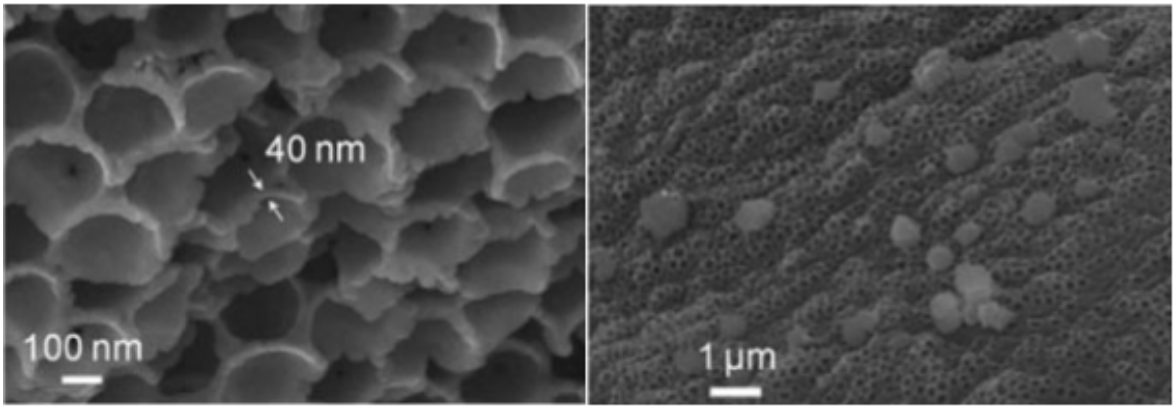

Figure 5: SEM images of the porous Si particles indicating a pore wall size of 40nm. [19]

Nanowire: Nanowires are fabricated using vapour-liquid-solid process directly onto the substrate. nanowires can also accommodate large strain without pulverization and provide good conduction pathway as each wire is directly connected to the current collector, in addition maintain high specific capacity over large number of charging cycles. Main stress alleviation is due to how the wires are arranged, providing space between adjacent nanowires to allow stable volume expansion during lithiation. No to mention that due to nano mechanics, nanostructures can undergo superplastic deformation and the dimensions of the nanostructure limit size of precursor crack thus handling large stress without failing or fractures. However, they are difficult and expensive to prepare compared to 3D pores. [18]

2.3. Honeycomb-structured Silicon:

2.3.1. Structural morphology

A robust architecture that can undergo countless Li-ion extraction/insertion cycles while retaining material integrity is now desired, especially the ability to withstand even more cycles than previously mentioned nanostructuring methods. The honeycomb structure's mechanical behavior was studied using scanning

electron microscopy (SEM) where the Honeycomb layered is supported on planar TiN covered Si substrate [5].

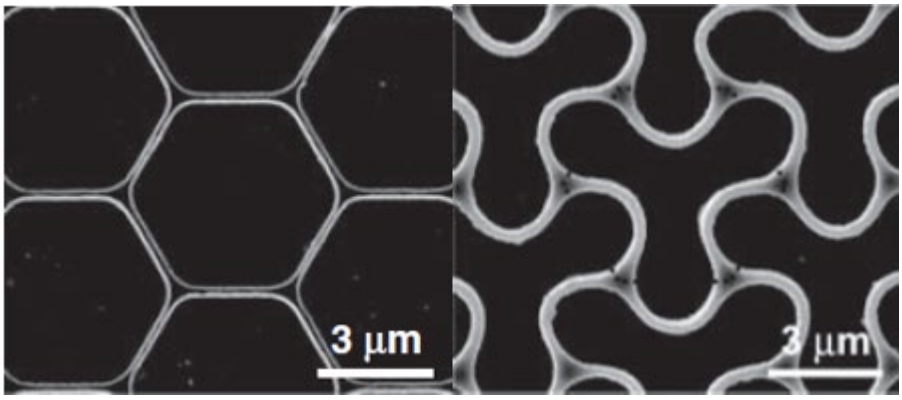

*Figure 6: SEM images of unlithiated **(left)** and fully lithiated **(right)** silicon honeycombs [5]*

The point where the walls (or vertices) of the honeycomb structure intersect is known as "triple points" and the closest distance between the triple points is 2.9µm. Due to the shape of the honeycomb structure, one may see the void between opposite vertices and that the material structure only occupies 10% of the geometric footprint area.

Key discoveries made with this structure is shown in figure 6, where the Si honeycomb structure morphed when exposed to Lithium content insertion, becoming extremely curved all while the triple points distance remain unchanged. As expected, the thickness and height of the vertices has increased noticeably compared to the pre-lithiated form and that opposite walls were bending in the same directions. And upon de-lithiation, the structure transforms back to its original form shown in pre-lithiation, indicating a reversible process.

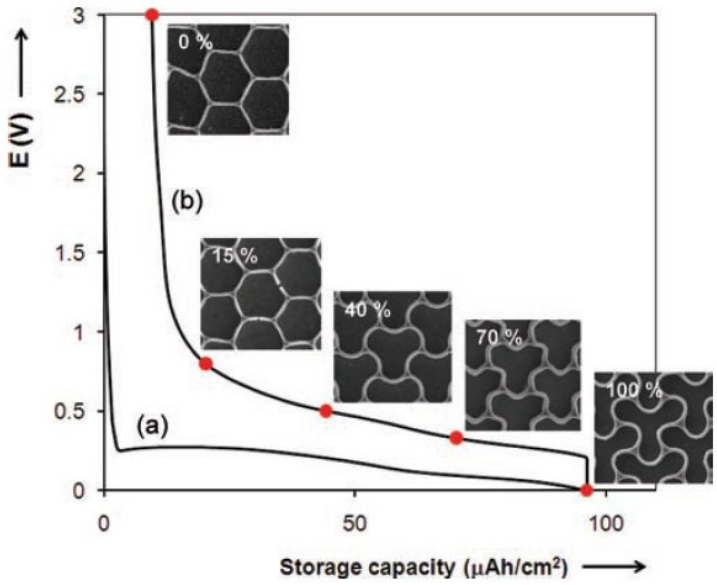

Figure 7: Morphological changes of the Si honeycomb structure as a function of Li content [6]

Figure 7 shows the morphological changes to the honeycomb structure which occurs when different Li-content is present in the structure. Where line (a) represents the lithiation cycle and (b) de-lithiation cycle. The SEMs presented above displays the reversible mechanical deformation of the Si honeycomb structure during the de-lithiation cycle. From 100% fully lithiated condition, the structure gradually straightens back to its original form, but even at 0% lithium content, it fails to convert back to being identical with its initial form, where now the vertices are slightly bent. Moreover, on closer inspection, at 15% Li content, it is apparent that the walls between the triple points cracked due to plastic deformation where it experiences stress most as one would expect when subjected to bending force.

It was also deduced that the surface coverage of the honeycomb structure increases linearly with Li content from 20% to 80%, which then flattens out after 80% due to thickening and bending of the vertices. However, the height increase of vertices has a different relationship with Li content present in the structure, where the height increase stabilizes at 30% Li content. Through this observation it is established that the honeycomb structure doesn't deform isotopically in 3D.

2.3.2. Capacity retention enhancement:

This specific structure can perform up to 30-50 cycles of stable storage capacity after which the capacity decreases drastically. Intuitively, modifying the honeycomb structure with more stable dimensions may increase cycle numbles with stable storage capacity. Since the expansion tends to happen in the direction where the vertices have the smallest dimension, this introduces wall bending and thickening to this area, thus decreasing the wall length to thickness ratio will lead to a lower wall bending when exposed to lithium, encouraging expansion in the direction perpendicular to the substrate. Lower degree of bending means less chance of cracking of the honeycomb vertices and increasing wall thickness contributes to a denser Si material so there is more storage capacity. Further research is required in designing a honeycomb nanostructure with optimum geometries to withstand the mechanical deformations as well as accommodating more Li content.

2.3.3. Vertices buckling model induced by chemical reaction

A more detailed qualitative investigation regarding the morphological deformation of the honeycomb structure was investigated, more specifically the structural element buckling between the triple points [6]. While the Si honeycomb structure is undergoing the electrochemical reaction mentioned in section 2.1, strains are induced by the two-phase electrochemical reaction at the sharp interface, accompanied with volume expansion of the structural elements at full lithiation. However, in this specific structure, the triple points act as external support/ loadings which restricts the deformation of the structural elements caused by internal stresses, leading to the stored elastic energy to be released via buckling.

At first one may think that buckling means loss the load-bearing capacity thus viewing it as a negative phenomenon. On the contrary, due to buckling, stresses may retard or block the chemical reaction acting as a stress mitigating mechanism in the structural elements of the vertices.

The elastoplastic deformation behavior of the honeycomb-structured Si based on a coupled structural–diffusional analysis was modelled numerically in [19] but the lithiation process was modelled as a non-stationary diffusion problem, meaning in this model lithiation of Si affects the internal stresses but not vice versa, whereas mentioned in section 2.2, the reaction rate can be blocked by internal stresses produced from the chemical transformation. The model created by in [6] accounted for the fact that lithiation reaction rate can be affected internal stress itself, and that the reaction is controlled by reaction rate and not by diffusion of reactant as mentioned in section. Therefore, generating a chemo-mechanical coupling model where the rotation of the vertices (between the triple points) in the honeycomb structure are modelled as a simply supported plate and the kinetics of the reaction is modelled in terms of a stress dependent chemical reaction using the chemical affinity concept. This concept generates a connection between the mechanical stresses induced and the reaction rate in a thermodynamically sound manner. An analytical solution was produced in [6] to demonstrate a scenario of stability consideration of the mechanochemistry problem, and the model was simplified to consider a small strain approach as well as linear elastic material properties.

2.3.4. Influence of the material and geometrical parameters on the buckling occurrence

During the modelling process, it was established that while the chemical reaction front propagates, the reaction forces at the support increases and that the bending stiffness of the plate decreases. Furthermore, the higher the chemical energy parameter γ is, the quicker for buckling will occur as shown in figure 8. Since energy parameter γ represents the chemical energies of the stress-free solid constituent of the reaction, if it is comparable to the contribution of mechanical energy, then the influence of internal stress on time until buckling becomes noticeable, reinforcing the fact stated above where that lithiation reaction rate can be affected by internal stress itself. If one would like to shorten time until buckling, one can increase the energy parameter by adjusting the temperature, however thermal stress may be produced which affects the overall reaction rate.

Nonetheless, in a viscoelastic case, stress may relax due to inelastic deformation instead. Even though buckling may not occur in this case, the reaction may still be temporary blocked by remaining stress, leading to an uneven reaction rate between the top and bottom of the vertices, possibly blockage at the top reaction front and retardation at the bottom reaction front. [20]

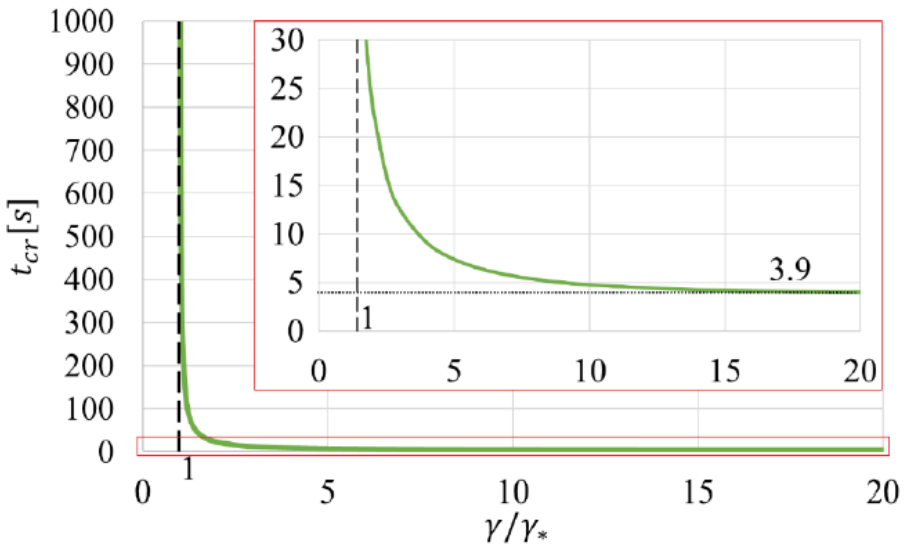

Figure 8: Dependence of the time until buckling on the chemical energy parameter [6]

2.4. Literature review conclusion

Overall, Silicon as a prospective electrode has demonstrated an increase in energy storage capacity compared to previous anode choices for LiBs. It could be commercially viable if the problems stemming from volatile volume expansion and stress induced deformation is overcome, in order to maintain the capacity stability over numerous lithiation cycles.

The two-phase lithiation mechanism was identified and it was shown that the propagation of the chemical reaction front is governed by the **i)** consumption of the diffusing reactant (The Si-Si bond breaking at the interface) at the reaction front and **ii)** the diffusion of a reactant in the body undergoing a chemical reaction, hinting that stress may affect the reaction front propagation by influencing the diffusion [22]. It was also demonstrated a-Si undergo a much more manageable physical transformation than c-Si during the first lithiation cycle.

Nanosizing methods such as nanowires and nanopores were then proposed to solve the limitations of cracking and pulverizations of the Si anodes during this repeated electrochemical process. Many ongoing novel methods have been devised for improving the Si's structural degradation resistance during this process and the Si honeycomb structure in particular shows promising performance in maintaining high specific capacity as well as possesses a unique stress relaxation mechanism, more specifically a reversible morphology of the whole structure. As a results this structure's vertices buckling occurrence was examined while coupling the stress on the model plate with the reaction rate via the chemical affinity tensor concept, additionally the influence of geometrical and material parameters on the buckling was also considered.

However, only analytical solutions assuming a linear elastic material property and small deformation was achieved in previous work regarding this structure. Therefore, Further efforts should be dedicated towards investigating the post-buckling behavior of the vertices, in order to get the full picture of the asymmetric problem and enable better understanding of the kinetics of the reaction front so that more realistic and accurate modelling could be commenced in the future.

3. Methodology/Design:

To model the ongoing deformation and chemical reactions in the vertices of the Si honeycomb structure during lithiation, the general problem is reformulated for the two-phase lithiation of a rectangular 2D beam upon the first lithiation cycle, thus essential constitutive equations as well as related computational formulations used in this model will be presented in this section. This problem will be simulated first using the linear elastic material model with small deformations approximation. Afterwards, large deformation and hyper elastic materials properties will be included to model the post-buckling behavior of the kinetics of the reaction fronts.

3.1. Chemical potential:

The aforementioned reaction front kinetics can be modelled based on the notion of the chemical potential [21]. It is known that the thermodynamic concept - chemical potentials are tensorial quantities in the context of deformable solids, the Eshelby tensor form of the chemical potential is used to help formulate criteria for phase equilibrium between material transformation phases of any symmetry. [22] The chemical potential being tensorial then leads to the fact that the chemical affinity is also tensorial, meaning that chemical reactions are also considered at an oriented surface area element which passes through a point as opposed to a reaction just at a point. [23] In the case of a propagating reaction front, the driving force is equal to the normal component of the chemical affinity tensor, which also equals to the combination of chemical potential tensors of solid constituents and the diffusing constituents. Through this approach, it allows one to understand that how mechanical stress affect the reaction rate via the chemical affinity tensor which will be demonstrated in section 3.3.

This paper's modeling process will utilize the framework based on kinetics of the reaction front being governed by the chemical affinity tensor to simulate the 2-phase lithiation induced deformations and the stress-affected reaction rates for small as well as large deformations of the 2D Si plate model shown in section 3.6.

3.2. Thermodynamic background:

Consider a solid body undergoing a chemical transformation caused by a chemical reaction. In the absence of equilibrium, the notion of the chemical affinity can also be related to the entropy production E[S] due to the chemical transformation process, which is equal to [24]:

$$E[S] = T^{-1} A \omega \quad \textbf{(1)}$$

Where T is the temperature and ω is the chemical reaction rate. The chemical affinity A where in a general case is expressed as:

$$A = n_{-}M_{-}u_{-} + n_{*}M_{*}u_{*} - n_{+}M_{+}u_{+} \quad \textbf{(2)}$$

Where n_{-}, n_{*}, n_{+} are stoichiometric coefficients, u_{-}, u_{*}, u_{+} are the chemical potentials per unit mass, M_{-}, M_{*}, M_{+} are the molar masses of the reaction components (where subscripts +, * and – refers to the initial solid material, diffusing reactant and solid reaction product respectively), and the case A=0 means chemical equilibrium. The affinity divided by temperature is the thermodynamic force and the chemical reaction rate is the thermodynamic flow. The thermodynamic flow depends on the thermodynamic force, therefore in the context of this reaction, the chemical reaction rate is a function of the affinity:

$$\omega = \omega(A) \quad \textbf{(3)}$$

Showing the influence of external actions on the chemical affinity affects the chemical reaction rate. Since the derivative of energy density with respect to number of moles is a scalar variable, the chemical potential and affinity can be also presented as scalar values. However, due to the observation of phase equilibrium or chemical reaction taking place at an oriented area element passing through a point shows the tensorial nature of the chemical affinity and potential as mentioned earlier. From this, one may also imagine the similarity to the concept of stress, where it is a scalar quantity when dealing with liquid and gas, but a stress tensor is utilized when analyzing solids.

3.3. Kinetics of the chemical reaction

It is worth noting that the derivation of the chemical potential tensor is based on a continuum mechanics approach where motion of the entire site with respect to solid is considered, instead of a motion of individual particles with respect to the site. A problem relating to a deformable rigid body with unknown internal boundary, whose position in the case of thermodynamic equilibrium contains the least Gibbs energy was considered. (The state of minimum Gibb's function is frequently interpreted to be the state of chemical equilibrium [25]). Which then lead to the conclusion that, on a thermodynamic equilibrium boundary, balance of scalar chemical potentials is replaced by the balance of the normal components of a chemical

potential tensor that is equal to the Eshelby energy momentum tensors divided by the reference mass densities. Also, in case of a quasistatic propagating interface, the thermodynamic force driving the reaction front motion is given by the jump of the normal components of the Eshelby tensor. [23] Consequently demonstrating the tensorial nature of chemical potential and affinity. This is important to know as the kinetic equation determining the reaction front velocity depends on the normal components of the affinity tensor and hence the variation of **(3)** could be presented as:

$$w_n = k_* c \left(1 - \exp\left(-\frac{A_{nn}}{R\,T}\right)\right) \quad \textbf{(4)}$$

Reaction rate at the area element with the normal **n** is given by w_n in **(4)**. Where k_* is the kinetic coefficient, c is the partial molar concentration of the diffusing reactant, R is the universal gas constant, T is the current temperature and A_{nn} is the normal component of the chemical affinity tensor. The normal component of the of the reaction front velocity V_n can be expressed in terms of the reaction rate from the mass balance at the propagating reaction front [24]:

$$V_n = \frac{n_- M_-}{\rho_-}\,\omega_n \quad \textbf{(5)}$$

Where ρ_- is the reference mass density of the initial constituent (untransformed material). The chemical reaction is accompanied with volume expansion, which stems from deformation due to chemical transformation and diffusion of the diffusing reactant. The Material B_- is on one side of the reaction front and material B_+ and B_* the other side. Initial elementary volume dV_- transforms into dV_+ and the diffusion adds extra volume of dV_* inside material B_+. Then the ratio of stress-volumes of materials on both side of the reaction front is given by:

$$J_{tr} = \frac{n_+ M_+/\rho_+ + \xi n_* M_*/\rho_*}{n_- M_-/\rho_-} \quad \textbf{(6)}$$

Where $dV_i = n_i M_i/\rho_i$ (subscript i is replaced with +, - or *). ξ reflects the deformational interaction between reactants B_+ and B_* which depends on the diffusion mechanism of $B_*$and saturation ability of B_+.

In case of small deformation, the transformation strain is given by $\varepsilon_{tr} = ({J_{tr}}^{\frac{1}{3}} - 1)$ and the transformation strain produces internal stresses which combined with external loading in turn affect the reaction rate.

Since the stresses and strains affect the reaction front kinetic via their influence on the chemical affinity tensor, it can be shown that neglecting the contribution of the pressure terms (acting on the diffusing constituent B_*) to the linear momentum balance equation at the reaction front in a quasi-static approach, the normal component of the chemical affinity tensor can be expressed as:

$$A_{nn} = \frac{n_- M_-}{\rho_-}\chi + n_* \; RT \; ln\left(\frac{c}{c_*}\right) \quad \textbf{(7)}$$

Here c_* represents the reference concentration of the diffusing constituent B_* and χ is defined by the contributions of mechanical and chemical energies denoted by [6]:

$$\chi = \gamma + \frac{1}{2}\boldsymbol{\sigma}_-: \boldsymbol{\varepsilon}_- - \frac{1}{2}\boldsymbol{\sigma}_+ : (\boldsymbol{\varepsilon}_+ - \boldsymbol{\varepsilon_{tr}}) + \boldsymbol{\sigma}_-: (\boldsymbol{\varepsilon}_+ - \boldsymbol{\varepsilon}_-) \quad \textbf{(8)}$$

where γ is the temperature-dependent combination of the chemical energies of the stress-free reactants and the reference energy of the diffusing constituent:

$$\gamma = \eta_- - \eta_+ + \frac{\rho_-}{n_- M_-} n_* \eta_* \quad \textbf{(9)}$$

η_- denotes the temperature dependent chemical energies of reactants, which leads to γ also depending on temperature. It is also assumed for constituent B_+ and B_-, the Helmholtz free energy can be represented as the sum of the chemical energy and strain energy [26]:

$$\rho_- f_- = \eta_- + W_- \qquad \rho_- f_- = \eta_- + W_- \quad \textbf{(10)}$$

Where $f_\pm$ is the mass density of the Helmholtz free energies of constituents B_+ and B_-, $\eta_\pm$ is the chemical energies of B_+ and B_- and $W_\pm$ is the strain energy density?

3.4. Key problem formulation/ statement:

3.4.1. Mechanical component:

Since the transformation strain during lithiation results in mechanical stresses which affects the reaction rate, one has the solve an equilibrium equation to find the stresses and strains. The Linear momentum balance principle, a generalization of newton's 2nd law in the context of continuum solid mechanics must be satisfied in every point in the continuum [27]:

$$\nabla \cdot \boldsymbol{\sigma} + \rho \boldsymbol{b} = \rho \boldsymbol{a} \quad \textbf{(11)}$$

Where ρb represents the body forces acting on the solid and σ represents the Cauchy stress distribution within the deformed solid. a is acceleration of the solid and ρ is the density of the solid. However, the problem is considered quasistatic, hence the equilibrium equation becomes:

$$\nabla \cdot \boldsymbol{\sigma} = 0 \quad \textbf{(12)}$$

The symmetric Cauchy stress tensor σ is to be satisfied within domains of constituent B_+ and B_-, with the boundary and interface conditions [6]:

$$\boldsymbol{u}_{\Omega_0} = u_0 \qquad \boldsymbol{\sigma}_{\Omega_1} = t_0 \quad \textbf{(13)}$$

$$[\![\boldsymbol{u}]\!]_{\Gamma} = 0 \qquad [\![\boldsymbol{\sigma}]\!]_{\Gamma} \cdot n = 0 \tag{14}$$

Where u_0 and t_0 equals the displacement and traction implemented at Ω_0 and Ω_1 from the outer surface of the body, also Γ is the reaction front. Operator ∇ is defined with respect to current configuration when being solved and the double square brackets denote the jump of the variable at the Γ. It is also worth mentioning the relationship between the traction vector and the Cauchy stress tensor with n as the normal vector of the arbitrary plane:

$$\boldsymbol{t} = \boldsymbol{\sigma} \cdot \boldsymbol{n} \tag{15}$$

The constitutive relationship between the constituent are as follow:

$$\boldsymbol{\sigma}_{-} = \boldsymbol{C}_{-} : \boldsymbol{\varepsilon}_{-} \qquad \boldsymbol{\sigma}_{+} = \boldsymbol{C}_{+} : (\boldsymbol{\varepsilon}_{+} - \boldsymbol{\varepsilon_{ch}}) \tag{16}$$

Where $C_{\pm}$ represents the stiffness tensors and ε_{ch} is the chemical transformation strain that could expressed as:

$$\boldsymbol{\varepsilon_{ch}} = \varepsilon_{ch}\,\mathbf{E} \tag{17}$$

Where **E** is a second order unit tensor. Equation **(17)** shows the chemical transformation tensor $\boldsymbol{\varepsilon_{ch}}$ is the chemical transformation scalar ε_{ch} multiplied by the identity tensor **E** and that ε_{ch} is a constant that will be presented in the model parameter (section 3.12).

3.4.2. Diffusion component:

The consumption of reactant B_* during the chemical reaction is governed by diffusion of the reactant through the transformed material B_+ to the reaction front. In this paper the diffusion flux is projected onto the reference configuration of material B_- and that we assume the diffusion process occurs a lot quicker than the velocity of the reaction front propagation. Then the stationary diffusion is described by [28]:

$$\Delta c = 0 \tag{18}$$

With boundary conditions of

$$D\boldsymbol{n} \cdot \nabla c + w_n = 0 \tag{19}$$

at the reaction front Γ mapped onto the reference configuration of B_- [6],

$$D\boldsymbol{n} \cdot \nabla c + \alpha(c - c_*) = 0 \tag{20}$$

at the outer boundary of constituent B_+ mapped onto the reference configuration of B_-. Here, D is the diffusion coefficient of B_* in material B_+ while α is the surface mass transfer coefficient. c_* denotes the solubility of reactant B_* in material B_+. Operator Δ is defined with respect to the reference configuration of

B_- and $\boldsymbol{n}$ is the normal directed outwards of material B_+. The boundary condition **(20)** is from the mass balance at the reaction front which implies that all diffusing reactant is consumed by the chemical reaction and the boundary condition **(19)** states that if solubility $\boldsymbol{c_*}$ is reached then the supply of diffusing reactant stops.

Since chemical equilibrium occurs at $A_{nn} = 0$ and the reaction front stops moving at this moment, the equilibrium concentration $\boldsymbol{c_{eq}}$ can be expressed below, in a given stress-free state as

$$A_{nn}|_{c=c_{eq}} = 0 \quad \textbf{(21)}$$

One can then deduce that A_{nn} as a function of the current reactant concentration c. Then boundary condition equation **(20)** at Γ can also be rewritten as [29]:

$$D\boldsymbol{n} \cdot \nabla c + k_*(c - c_{eq}) = 0 \quad \textbf{(22)}$$

Consequently, the current concentration can be found by using equation **(18)** with the boundary condition of equation **(22)** above. The equilibrium concentration is then determined by the stress and strains at the reaction front from using equation **(21)**, which the stress and strains are in turn determined by the mechanical equilibrium stated in **(12)**. However, in this model the concentration is assumed to be at saturation level to simplify the problem.

3.5. General problem-solving procedure:

Firstly, stress and strains are found from solving the equilibrium equation **(12)** depending on geometrical parameters, then they are substituted into equation **(8)** to obtain the chemical affinity tensor A_{nn}. Subsequently, the equilibrium concentration c_{eq} is determined using equation **(21)**, so that the dependence of c_{eq} on the geometrical parameter of the reaction front position is also found. The current concentration at Γ is found through equation **(18)** with boundary condition **(22)** also as the function of the geometrical parameters at the reaction front. Once both concentrations are found, the reaction rate could be obtained so that the time evolution of the reaction front could be found with the reaction front velocity equation. Therefore, one has a coupling between mechanics, diffusion and the chemical reaction to describe the reaction front.

3.6. Specific model architecture:

The general problem is reformulated for the two-phase lithiation of the vertices in the Si honeycomb structure upon the first lithiation cycle. The geometry of the model is an idealized 2D rectangular beam, depict a single wall between 2 triple points in the Si honeycomb. We consider this 2D plate to undergo the chemical reaction:

$$n\_Si + n_*Li \rightarrow Li_{n_*}Si_{n\_} \quad \textbf{(23)}$$

Above chemical formula shows the chemical reaction where a-Si inside the walls of the honeycomb is transformed into Li-Si solid upon the insertion of Li-ions during the lithiation process.

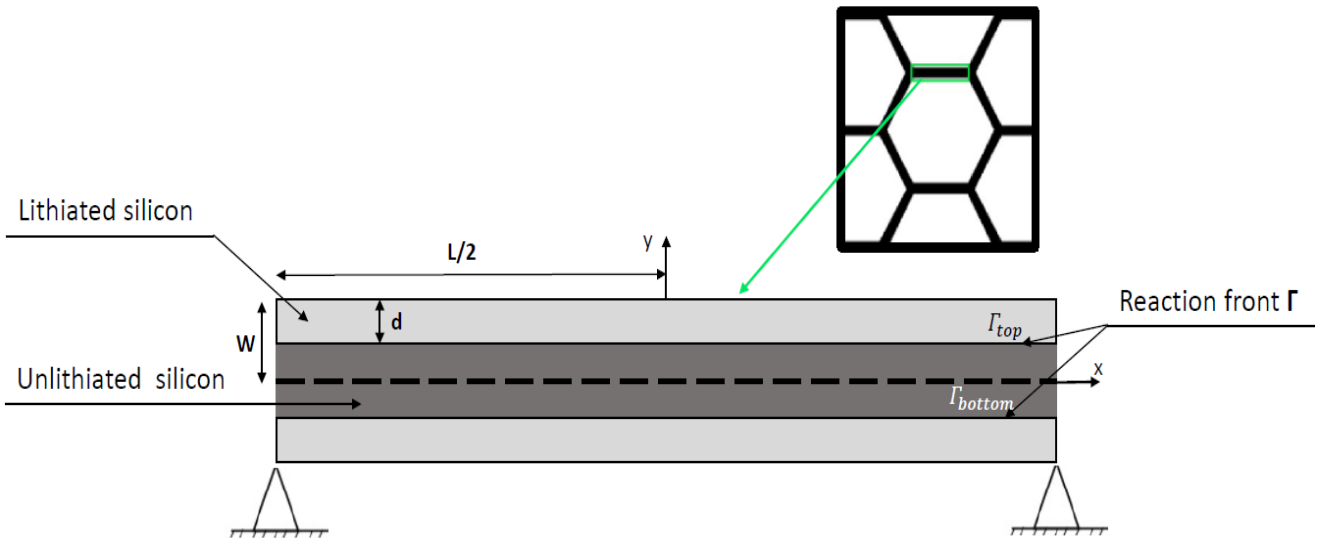

Figure 9: Schematic representation of the 2D plate model

We consider a plate of length L and thickness 2W undergoing the lithiation process and the lithiation is localized at the reaction fronts which form transformed rectangular layers after the chemical reaction. The plate is simply supported at the edges along the $x = \pm L/2$ and has a width (out of plane) of B. The upper and lower sides (external surface of the plate) $y = \pm W$ are traction free, with the diffusing reactants being supplied through the upper and lower sides. The chemical reaction initiates simultaneously from both sides and propagates towards the middle core/layer which is a layer of unlithiated a-Si. Hence the transformed layers from top and bottom is separated from the a-Si layer by the chemical reaction fronts of Γ_{top} and Γ_{bottom} (represents the top and bottom reaction fronts). Also in this model, it is assumed that initially the top and bottom transformed material layers have the same thickness d and the plate is symmetric with respect to the middle plane y, but as the reaction commences the transformed layer thickness may turn asymmetric.

The boundary and interface conditions equation **(14)** in this model take the following form:

$$[\![\boldsymbol{\sigma}]\!]_{y=\Gamma(top\ \&\ bottom)=\pm(W-d)} = 0 \quad \textbf{(24)}$$

Since upper and lower surfaces are traction free, the traction continuity condition holds true at both reaction fronts as well as the displacement continuity condition:

$$[\![\boldsymbol{u}]\!]_{y=\Gamma(top\ \&\ bottom)=\pm(W-d)} = 0 \quad \textbf{(25)}$$

In this model, we also assume the current Li concentration is at the saturation level (c = c*) thus the normal component of the chemical affinity tensor equation **(7)** is rewritten as:

$$A_{nn} = \frac{n_- M_-}{\rho_-}\chi \quad \textbf{(26)}$$

This assumption neglects the diffusion process's effect on the chemical affinity tensor which in turn, doesn't affect the reaction front propagation velocity. Lastly, new position of the reaction fronts in the 2D plate coordinate is determined by integrating the stress-dependent reaction front velocity:

$V_n = \frac{dy_\Gamma}{dt}$ where V_n is always positive in the linear elastic model. **(27)**

Further, we assume a plain strain formulation with B (dimension in z- direction) being much larger than L and 2W (dimension in x and y direction) hence all strain components in the z-direction vanish, $\varepsilon_z{}^{\pm} = 0$. E.g. when determining the mechanical energy contribution χ, the component $\sigma_-:(\varepsilon_+ - \varepsilon_-)$ becomes $\sum_{i=1}^{2}\sum_{j=1}^{2}\sigma_{-ij}(\varepsilon_{+ij} - \varepsilon_{-ij})$. Accordingly, the chemical expansion applied in the Abaqus model will also be orthotropic.

3.7. Computational Method

The numerical simulation of the structural behavior of the lithiated 2D beam is carried out by utilizing the finite element tool Abaqus/Standard to solve above equations and the verification of the analysis is done by exploiting the analytical solution from [6] Abaqus also has the ability to simulate non-linear physics behavior which is useful for the large deformation prediction. However, in order to account for the propagating reaction front, a python script was written which automatically retrieves results from Abaqus per increment and calculate new reaction front height from the chemical kinetics equations gathered above, as the object-oriented language Python has been embedded within the Abaqus software product.

The approach to conduct the small deformation simulation is shown in figure 10, which consists of 4 main stages. The python script is the main component that controls the whole process, where all the boundary condition, model parameters as well as automatic iterations commands are stored. Firstly, the model parameters are inputted into the script, then the script creates an entire model part possessing requested material properties and analysis instructions. Moreover, boundary conditions, constraints and load is also applied onto the model through the script. Afterwards, the script will submit the input file created from the model to the Abaqus solver to run the analysis. Once the analysis is complete, the script will extract the

results from the analysis's output database file, which are mainly the stress $\sigma_{\pm}$ and strains $\varepsilon_{\pm}$ of both lithiated Si and un-lithiated Si layers at the position of the reaction fronts Γ_{top} and Γ_{bottom}.

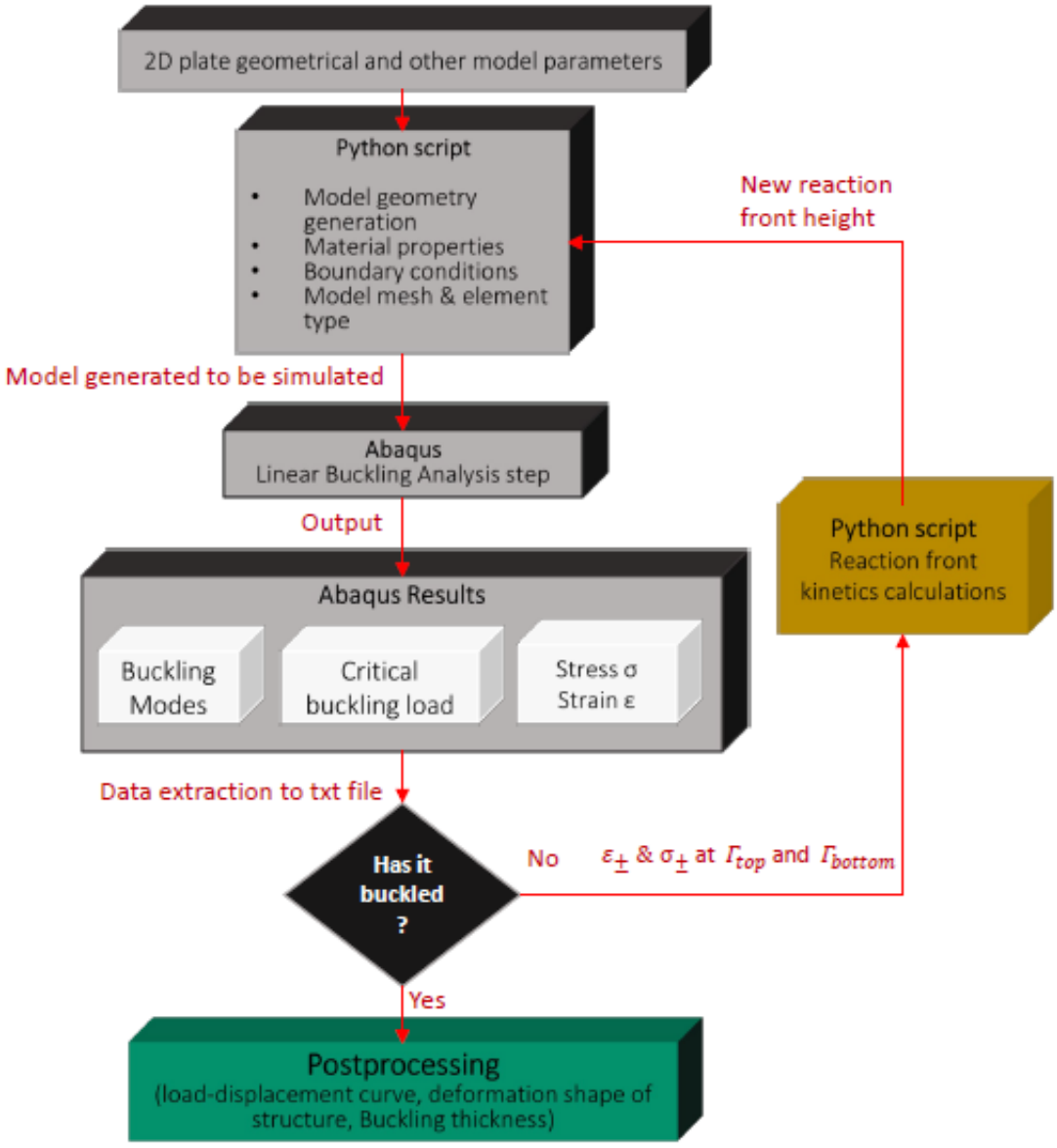

Figure 10: Schematic of the Linear elastic material model that predicts thickness of lithiated layers in the plate which induces buckling

The script then determines if the plate has buckled, if it buckled the script will proceed to the postprocessing stage where the critical buckling reaction front thickness is found; if the plate hasn't buckled, the extracted stress and strain will be used to calculate the new reaction front height with the reaction front kinetics equation **(5)** within the script, hence an entirely new model will be created with the new reaction height as a new mesh is required due to different geometry, and then resubmitted for processing. This process is

repeated until the transformed layer thickness that produces reaction force which induces buckle is found, and a new model represents a new time step Δt. This essentially removes the need to manually use the preprocessing module of CAE every time to create a similar model with just a small change in geometry.

3.8. Abaqus configurations:

3.8.1. Boundary condition and constraints:

To produce a model that demonstrates the most realistic deformation possible, a hinge boundary condition is applied. Ideally, the model should output homogenous stresses along the length of the reaction front due to uniform bending and this attribute of the deformation allows the entire reaction front to move together simultaneously (in a flat manner) all while neglecting the tiny fluctuations of stresses.

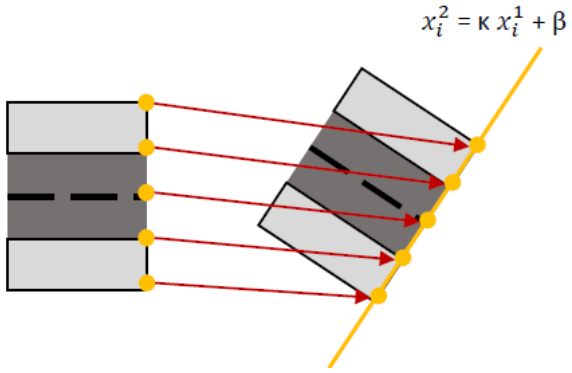

Figure 11:Visualization of the desired constraints equation

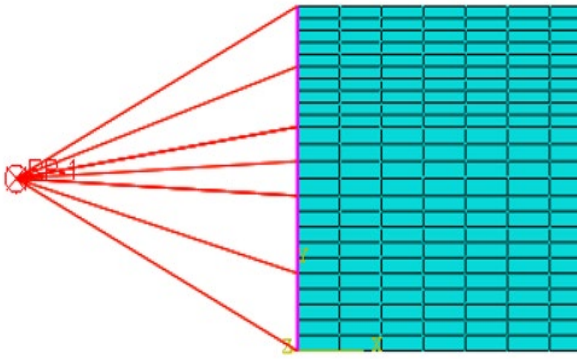

Figure 12: Snapshot of the continuum coupling constraint

The hinge boundary condition allows the left and right edges of the plate to rotate along a point that is an arbitrary distance away from the edge, shown in figure 12. Not only does this allow one to maintain homogenous stress along the reaction fronts but also imitates the realistic bending of beams between the triple points shown in figure 6. This is achieved by creating a reference point at an arbitrary distance away from the side of the beam, and then prescribing a displacement boundary condition on the reference point that restricts its displacement in u1 and u2 direction. Then a continuum distributing coupling constraint is applied between the reference point and the side edge, which constrains all nodes on the side edges to the rigid body motion of the of a single reference point, removing the need to manually input non-linear boundary hinge constraints into the equation constraint section in the GUI.

Another constraint is applied to the model which requires all nodes on the side edge to remain on a single line after deformation (even when chemical expansion is applied, nodes can expand along the same line freely.), derived in the standard form below:

$$(X_1^2 - X_2^2)u_i^1 + \left(X_2^2 - X_i^2\right)u_1^1 + (X_3^2 - X_1^2)u_2^1 = 0 \quad \text{Where } i\text{= 3,4,5…N} \qquad \textbf{(28)}$$

For the nodal displacement variable u_p^f, subscript p denotes the node number and superscript f represents the degrees of freedom (DOF). The original position of node p is expressed as X and degree of freedom 1 & 2 represents horizontal and vertical DOF. During the derivation for this constraint equation, the equation is linearized by neglecting higher order displacement terms. Assuming that the displacements are small, then the product of the small displacements will be of even smaller magnitude and are therefore disregarded. In general, there are N nodes and originally there is 2N DOFs, thus to make them deform on the same line it is required to constraint N-1 degree of freedoms, hence in total there is N-1 constraint equations that will be automatically inputted into the model via the python where N depends on the element density of the beam.

The python script is coded to take the stresses and strains from the integration points of the elements which are ± 1 element size away from the reaction's fronts, so that one may fully capture accurate stress and strain in both transformed and untransformed layers. Also due to the boundary condition, a constant curvature deformation will be observed, and is approximated to have constant stress values along the interface, therefore the script takes all the values along the length of the beam and average them, to then substitute the values into the reaction kinetics calculations.

In our Abaqus model, the plate in figure 9 is modelled in 2D plane. The solid plate continuum is discretized fully using an assembly of continuum elements of arbitrary quadrilaterals which are interconnected with other elements only at the nodes or vertices, the specific element type used in this model is 4-node bilinear element, with hourglass control (CPE4R).

3.9. Small deformation simulation:

The structural stability of the 2D plate is studied to observe the chemical reaction's effect on the mechanical behavior of vertices from the Si honeycomb structure. This is done by predicting the critical thickness of the transformed layer that induces buckling of the lithiated plate through computer simulation. Such study requires an eigenvalue buckling analysis from Abaqus. The eigenvalue buckling analysis outputs the associated buckling modes as well as an estimate of the critical load at which the response of the structure will bifurcate (if the response prior to bifurcation is linear) by investigating singularities in a linear perturbation of the structure's stiffness matrix in this general problem:

$$K\,u = 0 \qquad \textbf{(29)}$$

Where K is the tangent stiffness matrix when loads (Could be thermal or pressure) are applied and u is the nontrivial displacement solutions. This analysis is also useful for locating the first critical point in a non-linear analysis.

3.9.1. Eigenproblem buckling technique

The base state of an Abaqus model typically contain a dead load P_0 and the conventional stiffness matrix corresponding to the base state K_0 , taking in account of the effects from the preload/deadload. But preloads are often zero in classical eigenvalue buckling problems. Live load λQ is then applied with eigen value λ as the magnitude of the live load and Q is the pattern of the live load. K_Δ represents the differential initial stress and load stiffness matrix due to incremental loading pattern Q.

The equilibrium state becomes unstable when the determinant of its tangent stiffness matrix is equal to zero (Matrix becomes singular). This is because if det K = 0, there exists a non-zero displacement solution that requires no additional force which in this case means buckling. Since loss of stability occurs when total stiffness matrix is singular, it is key is to find values of λ which provide singularities in this tangent stiffness within the eigenproblem:

$$(K_0 + \lambda K_\Delta)u = 0 \quad \textbf{(30)}$$

Where $(K_0 + \lambda K_\Delta)$ is the tangent stiffness matrix when loads are applied. By seeking the eigenvalue λ aka loading factor that will bring the system's determinant to zero, a nontrivial solution to this problem is provided, which then defines the critical buckling load as $P_0 + \lambda_{cr}\, Q$ with the corresponding buckling mode. The script is designed t keep on calculating new height using the reaction front kinetics equations until the λ value output = 1, then it will exit the loop and display the critical transformed layer thickness that produced this load.

The subspace iteration method eigen solver type is selected as it is faster when only a few (less than 20) eigenmodes are needed compared to Lanczos where it is more suitable for large number of eigenmodes are required, also the Lanczos method in Abaqus cannot be used with a model containing distributing coupling constraints.

3.10. Large deformation simulation:

To capture further kinetics of the reaction fronts during the post-buckling process in the two-phase lithiation, a whole new simulation model was created after the small deformation simulation procedure, and it is designed to capture large deformations in nonlinear regime. The model architecture is similar to that of the linear elastic material model but key differences are the material parameters and the analysis step, moreover it is impossible to compare the large deformation simulation results to analytical solution.

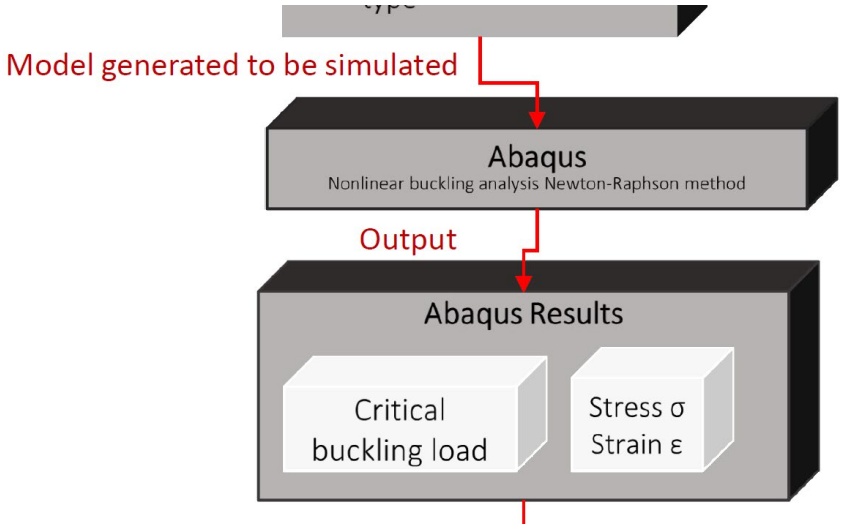

Figure 13 Updated schematic of the model for the hyperelastic model

As mentioned before Si can expand up to approximately 400%, and [5] showed that the honeycomb structure returns to its original shape during di-lithiation, responding elastically when subjected to very large strains hence intuitively hyperelastic constitutive laws are also used to model this Si honeycomb. It is a suitable material model as it accounts for both non-linear material behavior and large reversible shape changes (50% or more) with almost zero plastic deformation before failure as illustrated in figure 6. Key difference between this model and the previous linearly elastic material model can be observed in stress-strain response where the hyperelastic model is highly nonlinear to the point where the previous elastic approximation is extremely inaccurate, especially when stiffness may be changing throughout the deformation. These inaccuracies may cause the simulation to predict stress that are very far away from the realistic stress needed for further strain hence hyperelastic model is applied to capture the post-buckling reaction front kinetics as it offers a closer approximation. However, in both hyperelastic case and the previous elastic case, work done on the structure are expected to be stored as internal energy and is fully recallable as long as deformation is elastic. Additionally, in this model the Si is considered as incompressible.

All hyperelastic material's constitutive behaviour postulates the existence of Helmholtz free-energy function, defined per unit reference volume. For the case where the Helmholtz free-energy is solely a function of F or a strain tensor of the Si, it is commonly referred as the strain-energy function:

$$\psi = \psi(\boldsymbol{F}) \tag{31}$$

In this model, we consider Si to be a homogenous material where the distribution of internal constituents are assumed to be unform on a continuum scale. The stress-strain relationship for a solid is defined by specifying its strain energy density as a function of the deformation gradient tensor F in the Si and J =

det(**F**). It is known that the stress response of hyperelastic materials is derived from the scalar-valued energy function, implying that the hyperelasticity has a conservative structure. The derivative of the scalar-valued function with respect to tensor variable F represents the second order tensor known as Piola-kirchoff stress tensor. The strain energy density (aka strain energy potential) is denoted by ψ in this model. If the strain density is a function of the left Cauchy-green deformation tensor **B**= **F**. $\boldsymbol{F^T}$, the constitutive equation is automatically isotropic and that **B** is used as the deformation measure, thus strain energy density is a function of the invariants of B and an invariant of a tensor doesn't vary as the reference coordinate system changes. The stress-strain law in this case is an equation that relates the Cauchy stress σ_{ij} to the left Cauchy-green deformation tensor F. For computation convenience, Kirchoff stress can be used as another stress measure where:

$$\tau_{ij} = J\ \sigma_{ij} \tag{32}$$

As mentioned above, the constitutive law of the isotropic hyperelastic Si model is then deduced by the partial derivative of the energy function with respect to the deformation gradient [26]:

$$\sigma_{ij} = \frac{1}{J}\frac{\delta W}{\delta F} \cdot F^T \tag{33}$$

The Cauchy stress tensor can be split into the hydro static stress and the deviatoric stress (Responsible for the distortion of the shape).

$$\boldsymbol{\sigma = \sigma_H + \sigma_d} \tag{34}$$

Where in this quasi-static loading, the hydrostatic load could be described as $\sigma_H = \frac{\sigma_{kk}}{3}$, which can be found by solving the equilibrium equations and that the deviatoric stress is the part of the stress tensor which is responsible for large deformations thus it is important to know for the invariants of σ_d

The volumetric terms will be connected to the Bulk modulus (Since hydrostatic stress is directly proportional to the volumetric strain) and the deviatoric part will be connected to the Shear modulus. There exist specific forms of strain energy densities and the generalized neo-Hookean model is used for representing the nonlinear elastic behaviors of the plate in this project:

$$\bar{U} = \frac{\mu_1}{2}(\bar{I}_1 - 3) + \frac{K_1}{2}(J-1)^2 \tag{36}$$

Where μ_1 and K_1 are material properties. The hyperelastic model is also solved using Abaqus where it automatically creates the response curves for the selected strain energy form. All hyperelastic models in the software are based on the assumption of isotropic behavior throughout the deformation history and the strain energy density is formulated as a function of the strain invariants. It is recommended that to use solid

continuum hybrid elements for almost incompressible hyperelastic materials with initial poison's ratio greater than 0.495. The Neo-Hookean model expressed in Abaqus is as follow:

$$U = C_{10}(\bar{I}_1 - 3) + \frac{1}{D_1}(J^{el} - 1)^2 \quad \textbf{(37)}$$

Where U is the strain energy per unit reference volume; $\bar{I}_1$ is the first deviatoric strain invariant defined as:

$$\bar{I}_1 = \bar{\lambda}_1^2 + \bar{\lambda}_2^2 + \bar{\lambda}_3^2 \quad \textbf{(38)}$$

With $\bar{\lambda}_i^2 = J^{-1/3}\lambda_i$, where J is the total volume ratio, J^{el} is the elastic volume ratio defined in the thermal expansion tab in Abaqus and λ_i are the principle stretches. The material properties inputted in the software are given by:

$$\frac{\mu_1}{2} = C_{10} \qquad \frac{2}{K_1} = D_1 \quad \textbf{(39)}$$

Where μ_1 and K_1 represents the initial shear modulus and bulk modulus. The Neo-Hookean model is used due to limited data to available and this specific form of strain energy density requires only 2 material parameters, the shear and bulk modulus. More material data is required to use other models such as the Mooney-Rivlin or Ogden [30]. Although the equation is linear, the invariant itself is a nonlinear function of strain thus it is still a nonlinear model.

The hyperelastic model also utilizes the general static step procedure in Abaqus with the nonlinear geometries' option switched on, this procedure then uses the Newton-Raphson method to solve the non-linear equations iteratively until the solution convergences. The propagation of the reaction front is modelled as change of the position of both reaction fronts by Δd each time step Δt. Since spatial step is fixed, time step is an additional unknown. The strain energies on are taken at the integration points of the transformed and untransformed constituents' elements on either side of the reaction front, which share the reaction front node, in order to calculate the propagation speed.

3.11. Model Parameters:

Parameter	E_-[GPa]	E_+[GPa]	ν_-[-]	ν_+[-]	k_*[m/s]	c_*[mol/m^3]	ε_{ch}[-]
Value	134	41	0.22	0.26	$8.6 \cdot 10^{-8}$	$5.3 \cdot 10^4$	0.05
Parameter	γ [J/m^3]	n_-[-]	M_-[Kg/mol]	ρ_-[Kg/m^3]	T [K]	W [m]	L [m]
Value	$4 \cdot 10^9$	$\frac{4}{15}$	$2.80855 \cdot 10^{-2}$	2285	293	$0.171 \cdot 10^{-6}$	$2.9 \cdot 10^{-6}$

Table 2: Model material parameters used in the simulations (Specific change in parameters value s will be specified)

This section summarizes the model parameters that were used to simulate the lithiation of the Si honeycomb wall vertices. There are in total 2 different materials in this prediction model, the transformed material

(lithiated Si) and the untransformed material (pure amorphous Si). The bulk modulus was calculated from the Young's Modulus $\boldsymbol{E}_-$ and the Poisson's ratio $\boldsymbol{\nu}_-$ taken from [31] using the relation $K_- = \frac{E}{3(1-2\nu_-)}$, the shear Modulus on the other hand determined by $\mu_- = \frac{E}{2(1+\nu_-)}$. The young's modulus $\boldsymbol{E}_+$ is taken from [32] where the mechanical behaviour of amorphous silicon was studied experimentally in the case of nanoindentation, and that the Young's Modulus was measured. The density of Si was taken from [33] and the dimensions of the 2D plate are $2.9{\cdot}10^{-6}m \times 0.342{\cdot}10^{-6}m$. Moreover, the solubility $\boldsymbol{c}_*$ with respect to the reference configuration of B_- is taken from [26]. The full list of parameters is provided in table 2 where all parameter values are presented in SI units.

4. Results and Analysis:

4.1. Linear elastic model – pre-buckling reaction front kinetics

4.1.1. Numerical model verification (1st Simulation run)

The key function of the linear elastic model in figure 10 was to predict the relative thickness of the transformed layer that causes the vertices to buckle. This was simulated using parameters from table but L and W are altered to $11.6{\cdot}10^{-6}m \times 0.25{\cdot}10^{-6}m$ instead for the 1st simulation run to enable comparison with [6]. The script was able to output the critical thickness of the transformed layer as 2.49nm for both top and bottom with a buckling time of 0.130 seconds. Correspondingly, this equates to a 0.0187 of relative thickness of the transformed layer ζ_{cr}, where $\zeta_{cr} = d_{cr} \,/\, W$. This result obtained from the numerical simulation is then quantitatively compared to the analytical solution developed in [6] where the buckling criterion - the equality of the reaction force and the critical buckling load, lead to the development of the following equation to determine the thickness of the transformed layer at which buckling occurs:

$$\left(\frac{C_-}{C_+} - 1\right)\eta_{cr}{}^3 + G\eta_{cr} + (1 - G) = 0 \qquad \text{where } \eta_{cr} = 1 - \zeta_{cr} \tag{40}$$

And the parameter G can be represented as:

$$G = 3\varepsilon_{ch}(1 + \nu_+)\frac{L^2}{\pi^2 W^2} \tag{41}$$

The calculated analytical relative thickness $\zeta_{analytical}$ was also 0.0187, which matches the numerical output completely, thus verifying the accuracy of the developed model script. Also this shows the symmetry of the problem with respect to the dotted middle plane in figure 9.

4.1.2. Stress and strain analysis (1st simulation run)

Note that the initial thickness of the transformed layer is tailored to be 0.4nm for this model, as the analysis is unable to initiate if the initial thickness on either of the reaction fronts (top or bottom) is less than this

value. The pre-buckling and buckling snapshots of the Si honeycomb vertices morphology is presented in figure 14.

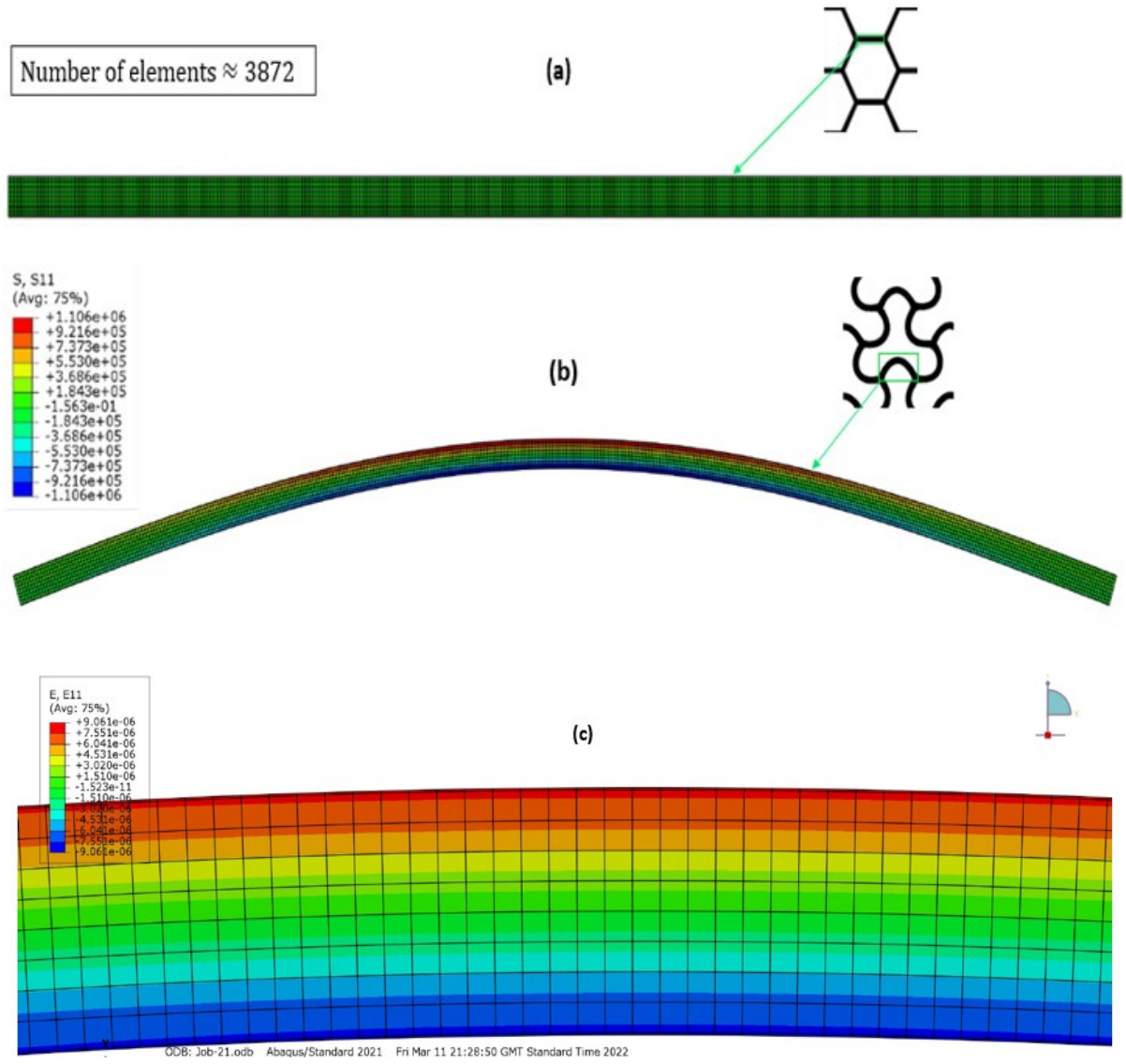

*Figure 14: Snapshots of the results obtained in the 1st simulation run **a)** Stress in 11 direction in the Stress-free state **b))** Stress in 11 direction in the buckling state **c)** enlarged view of strain in 11 direction (to enhance visualization due to high element density)*

The morphology of the vertices between the triple points were successfully simulated in the analysis, the distributions of the stress in the x-direction are shown in figure 14b and it can be seen clearly that the untransformed region (a-Si region) is stress free. Additionally, it is obvious that tensile stress gradually increases from the middle plane of the plate towards the top edge of the beam, with a maximum tensile stress. Correspondingly, due to the bending direction, there is a gradual increase in compressive stress from the middle plane towards the bottom of the plate caused by the volumetric expansion from the chemical

reaction. This agrees with the x-direction strain displayed in figure 14c where the top region above the middle plane is experiencing tensile strain and the bottom getting compressive strain as one would expect.

The top and bottom reaction front propagation speed was also found to be changing as the relative thickness ζ increases. Γ_{top} seems to be decelerating while the bottom reaction front is accelerating but the change in magnitude is of am/s (atto meters per second, order of 1E-18), therefore this change is not further investigated due to magnitude of change and that both reactoin fronts are considered to be travelling at a constant speed of 14.9 nm/s towards the middle plane until buckling occurs in the linear elastic material model.

4.1.3. Buckling Behaviors of plate with experimental geometries (2nd simulation run)

The model is also used to predict the buckling thickness for the Si honeycomb that was experimentally inspected with SEM in [5],therefore the dimensions from the table 2 is inputted in this simulation run. The mesh contained a total of 1626 elements and the initial thickness of both transformed layers are set to be 15nm in order to initiate the analysis. The model was able to output a buckling thickness of 52.3nm, which correlates to a relative thickness ζ of 0.305, moreover it took 2.6 seconds to buckle. Again, using the analytical solution a relative thickness $\zeta_{analytical}$ of 0.309, showing a 1.29% relative error between the numerical and analytical solution. This systematic error stems from how the model script was designed, the iterative loop stops when the new heights of the reaction front outputs an eigenvalue λ from Abaqus's eigen buckling step that is $\lambda < 1$, this means that the ζ_{cr} will not be exact, this could be fixed by decreasing the timestep to achieve a more accurate result but due to the time required per simulation run, the current time step set in the script is able to output a ζ_{cr} that is $\pm 3\%$ of the $\zeta_{analytical}$.

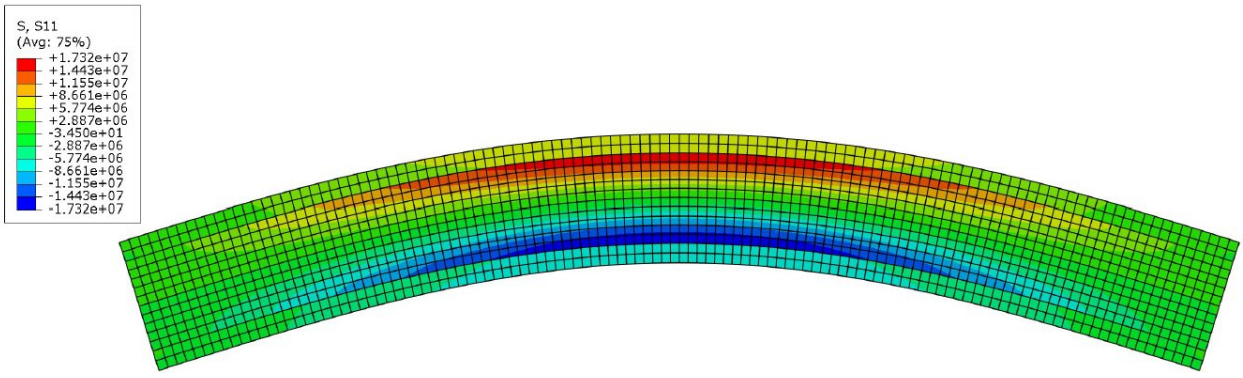

Figure 15: Snapshots of the stress in 11 direction obtained in the 2nd simulation run (New dimensions) in the buckling state

The deformation scale factor was set to 291 to enhance visualization of the buckling shape. It could be seen from figure 15 that the tensile and compressive stresses are no longer concentrated at the top/bottom edges of the beam but distributed along the reaction front for both sides while the transformed layers experience no stress. This reinforces previous research as it demonstrates that the chemical reaction is localized at the

sharp reaction interfaces, and where newly created Li_xSi at the reaction front pushes out previously transformed layer leading to tension on the surfaces, moreover the bending shape is what establishes the stress type. Additionally, the untransformed layer has a higher Modulus of elasticity meaning it is the stiffer material, so there will be less compressive/tensile strains in the unlithiated layer compared to the lithiated layer.

4.1.4. Reaction front kinetics (2nd simulation run)

The main purpose of this project was to model and observe the behavior of the reaction fronts in the during buckling hence the reaction front propagation velocity as a function of the relative thickness of the transformed layers (both top and bottom) is plotted in figure (16) for various values of the chemical energy parameter **γ.**

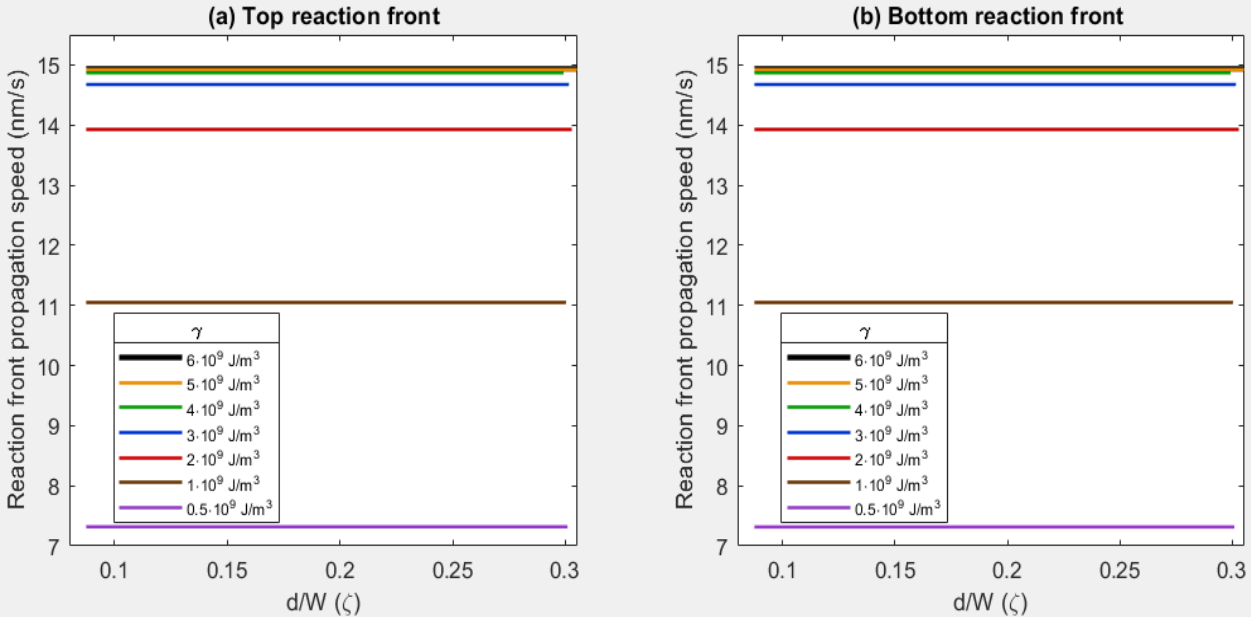

*Figure 16: The dependence of the reaction front velocity on the relative thickness of transformed layer at various values of the chemical energy parameter **γ a)** top rection front **b)** bottom reaction front in the 2nd simulation run*

It is obviously identified that a higher γ results in a greater reaction front propagation speed, this is expected due to equation **(8)**. If γ is too large to be comparable to the contribution of the mechanical energy, then the internal stresses are too miniscule to influence the normal component of the chemical affinity tensor, and the term $\exp\left(-\frac{A_{nn}}{R\,T}\right)$ in equation **(4)** tends to 0, and the reaction front velocity may become only proportional to the concentration of the reaction. Since the concentration term c_* in this model is a constant value, the reaction front propagation speed won't change either, which is exhibited above where the propagation speed appears to be approaching a limit of 15nm/s as γ tends to infinity. All simulations in this model are ran with 1/10th of a second timesteps, consequently a higher γ will lead to arriving at the critical relative thickness in less time. The **γ** value of $0.5 \cdot 10^9\ J/m^3$ did show a decrease in propagation

speed as it moves towards the center but like the previous simulation run, the change in magnitude is of pm/s (Pico meters per second, order of 1E-12), so the minor fluctuations were discounted. Nonetheless, it hinted that a smaller $\boldsymbol{\gamma}$ is required to exhibit the influence of internal stresses on the propagation as the stresses in this regime is a lot smaller compared to large deformation.

4.2. Hyperelastic model - post-buckling reaction front kinetics

4.2.1. 3rd simulation run

Further kinetics of the reaction fronts in the Si honeycomb vertices has not been captured either visually through experiment nor documented numerically, as such the asymmetric behavior of the kinetic reaction fronts during the postbuckling regime is analyzed with the developed hyperplastic model as mentioned in section 3.11 of the methodology. The reaction front velocity profile for the case of $\gamma = 5 \cdot 10^9\ J/m^3$ in the post-buckling regime indicated a similar situation to the pre-buckling of the plate such that there was no velocity drop witnessed (identical speed of 14.92 nm/s for both reaction fronts) due to γ being too large even in the post buckling stage, leading to a stress independent lithiation process. This makes sense as the blocking effect originates from the competition between the mechanical and chemical parts of the chemical affinity tensor, in this case stresses are neglected in the expression. The reaction fronts in this simulation trial propagated towards the center to the point that reaction fronts advanced past the middle plane and was overlapping with each other, producing an unrealistic outcome. Previous analysis suggests that a much smaller γ may reveal a more pronounced stress dependent lithiation process, therefore next few γ simulated were chosen such that it ranges from $0.1–0.05$, and that hyperelastic model script only ends the iterative process when Abaqus reaches its operational limit. As anticipated, the case of $\gamma = 0.1 \cdot 10^9\ J/m^3$ successfully showed a more stress relevant velocity profile compared to any of the previous runs.

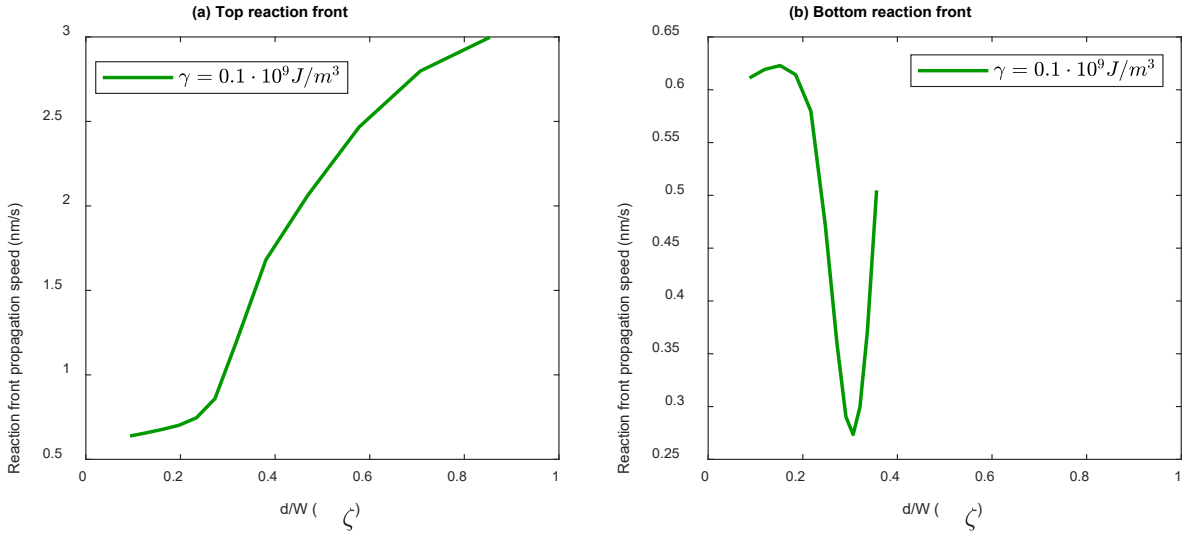

*Figure 17: The dependence of the reaction front velocity on the relative thickness of transformed layer a chemical energy parameter $\boldsymbol{\gamma}$ of $0.1 \cdot 10^9\ J/m^3$ for **a)** top rection front **b)** bottom reaction front in the 3rd simulation run*

Γ_{top} propagation profile was showing an increase in velocity as it moves towards the center and terminates at ζ = 0.854, not to mention the acceleration starts to decrease around ζ = 0.38 thus presenting a non-monotonic velocity profile. Correspondingly, the bottom propagation speed demonstrated an intial increase in speed until ζ = 0.152, then the propagation speed decelerates until ζ = 0.306 and was only able to advanced to ζ = 0.356. The acceleratoin anomly following the deceleration at ζ = 0.306 could be consdiered as a miniscule flucartion since the overll scale of the bottom propagatino vloecity is less than 1nm/s, so it is reasonable to assume the bottom reaction front is travelling at constant velocity, nonetheless this should be further investigated by setting a smaller time step to capture this phenomenon comprehensively.

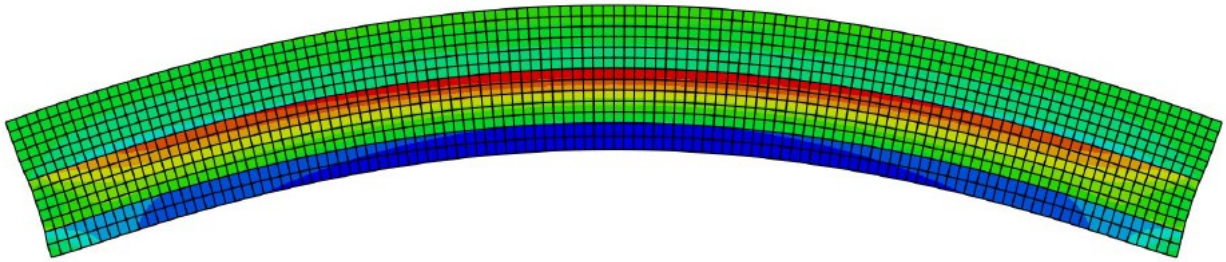

Figure 18: Snapshot of the stress in 11 direction obtained in the 3rd simulation run with the plate in the post-buckling state

In general, the case of $\gamma = 0.1 \cdot 10^9\, J/m^3$ showed the post buckling scenario with Γ_{top} accelerating while the bottom front decelerates after an initial acceleration as demonstrated in figure 18, where the Γ_{top} is near the middle plane and the bottom reaction front covered relatively less distance. This then results in large amount of tensile stress located near the middle plane of the plate and extremely concentrated compressive stress at the bottom of the plate, unlike in the 2nd simulation run where the reaction fronts propagated symmetrically. Therefore, the asymmetric reaction kinetics in the post-buckling regime was successfully simulated but it is interesting to note that none of the reaction fronts have a negative propagation velocity, so both will propagate towards the middle plane until the plate is completely lithiated with a gradual decrease in velocity, this can possibly be attributed to the initiation of the blocking of the reaction for the bottom reaction front. As one may see unlike in the linear elastic material model, the edges in the hyperelastic model were not flat after deformation even though the same constraint equation was applied, this is suspected to be the effect of linearizing the constraint equation during derivation of **(28)**

4.2.2. 4th simulation run

The behavior for the case when $\gamma = 0.08 \cdot 10^9\, J/m^3$ varied considerably compared with $\gamma = 0.1 \cdot 10^9\, J/m^3$. Γ_{top} demonstrated a similar stabilization of velocity, with a lower acceleration. However, the bottom reaction front yields a distinctive velocity profile where the propagation started with a positive

velocity 0.22nm/s then it keeps decelerating until it reaches a negative velocity of -0.317 nm/s, accompanied with first an increase in relative thickness and then a decrease from the relative thickness of 0. 189.

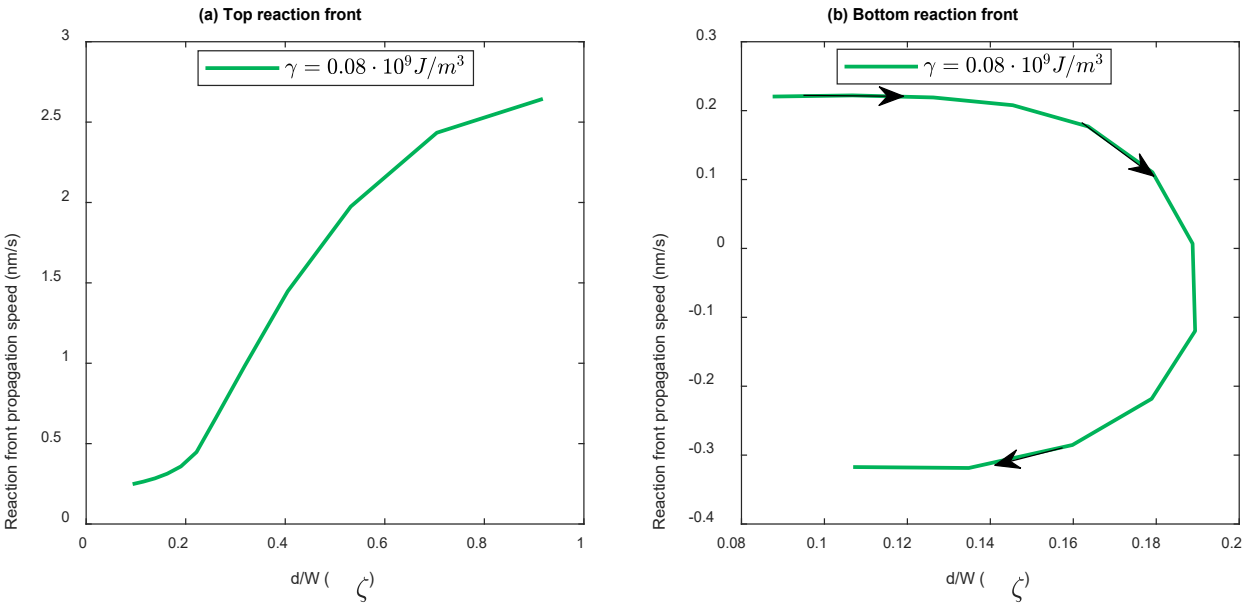

Figure 19: The dependence of the reaction front velocity on the relative thickness of transformed layer a chemical energy parameter γ of $0.08 \cdot 10^9\ J/m^3$ for a) top rection front b) bottom reaction front in the 4th simulation run

This is significant as it shows the scenario where initially both reactions fronts move towards the middle plane, until the plate buckles, then Γ_{top} continues to propagate until it reaches a relative thickness of 0.917 (Due to the operational limit of Abaqus), whereas the bottom reaction front starts to change direction and regresses back towards the bottom edge.

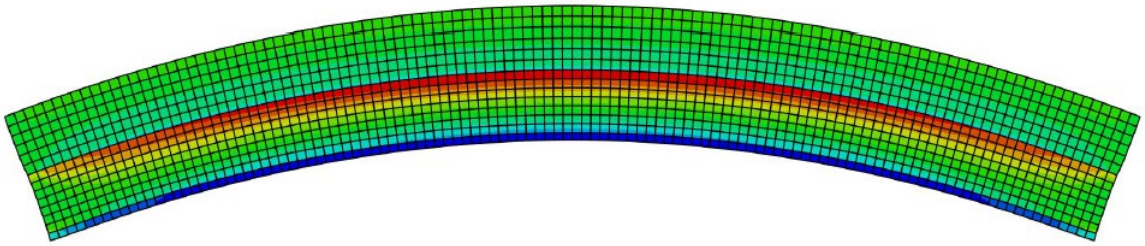

Figure 20: Snapshot of the stress in 11 direction obtained in the 4th simulation run with the plate in the post-buckling state

Compared to the 3rd simulation run in figure 18, the influence of stress on the reaction front kinetics was even more obvious as exhibited in figure 20, where Γ_{top} moves even closer to the middle plane and the bottom compression stresses are barely visible due to the regression of the bottom reaction front. These results qualitatively correspond to the experimental evidence where in a nano wire the lithiation process proceeded a lot quicker on side experiencing tensile stress than the compressive side, breaking the

symmetry of the propagation kinetics [34]. If the bottom reaction front is exposed to extremely high compressive stress, this would lead to lead to the term $\exp\left(-\frac{A_{nn}}{R\,T}\right)$ in equation **(4)** to be positive, resulting in a negative propagation velocity, thus realizing that compressive stress suppresses lithiation. It was also discovered that for $\gamma = 0.05 \cdot 10^9\, J/m^3$, both reaction front velocities started negative, which is impossible as reaction front cannot regress at the edge of the plate. Thus, realizing if γ is below a certain threshold value, the chemical reaction will not start.

5. Conclusion:

In this report, the stress-affected two-phase lithiation kinetics in the vertices of a honeycomb-structured Si undergoing buckling was studied. 2 coupled chemo-mechanical models were created by combining the concept of chemical affinity tensor with a linearly elastic model and a hyperelastic model. Python scripts were developed to simulate the chemically induced buckling process of a plate that represents the vertices of the anode honeycomb structure, for both regimes. The model scripts solve the problem using a finite element approach to predict the propagation of the top and bottom reaction fronts as well as the stress-strain states during the lithiation of the plate.

The buckling thickness (of the transformed material) predictions from the model were verified and the evolution of the stresses during the reaction front propagations were considered in detail. In both elastic and hyperelastic cases, due to the buckling mode shape, the stress in the transformed material is tensile at the top reaction front and compressive at the bottom reaction front. Moreover, the top and bottom reaction front kinetics were symmetric with respect to the middle plane up to the point of buckling in the linearly elastic simulation. Furthermore, it was proven that the thickness of the transformed layer which induces buckling depends on the thickness:length ratio. However, the linear elastic model is not valid in the post-buckling region, consequently the hyperelastic model was deployed. Although the buckling mode shape remained the same exhibiting tensile stress at the top reaction front and compressive stress at the bottom, due to the large deformation, the reaction front kinetics became asymmetric with respect to the middle plane, thus transformed layer thicknesses were different and stresses were not distributed uniformly from the middle plane towards the top and bottom of the plate during post-buckling.

The influence of mechanical stresses on the kinetics of the reaction front was shown at various values of the chemical energy parameter. The bias of lithiation rates due to the asymmetric stress profile had been observed experimentally, but the developed hyperelastic model was able to capture the retardation of the bottom reaction front which could only be achieved beyond the capabilities of analytical techniques.

Some limitations to this model include that realistically the reaction front will not move as a flat surface, each specific points along the reaction fronts will have different propagation velocity. Not to mention the problem was solved in a plane strain setting, thus all z-direction strain components in the strain tensor were neglected while physically the material expands volumetrically. On top of that, there is especially low confidence in the parameter γ as it is incredibly hard to measure and may impact on the reaction front kinetic accuracy. Additionally, this model doesn't resolve for plasticity due to time limitations.

More research is still required to fully predict the lithiation kinetics of the honeycomb-structured Si thus further efforts should be devoted to modeling the problem in 3D, because realistically the Si honeycomb structure maybe placed on the deck of a current collector, depending on the height of the structure in the z-direction, the bottom layer may be fixed to the deck while the top layer is more flexible so the degree of bending of the vertices in the honeycomb may vary throughout the structure. Furthermore, Silicon maybe modelled more accurately with viscoelasticity rather than hyperelasticity. Nevertheless, the results of this paper may be constructive towards designing Si honeycomb structure-based anodes in future LiBs.

6. References

[1] United States Department of Energy,Alternative Fuels Data Center, "Batteries for Hybrid and Plug-In Electric Vehicles," 2020. [Online]. Available: https://afdc.energy.gov/vehicles/electric_batteries.html. [Accessed 2022].

[2] United Nation, "Paris Agreement," 2015.

[3] Climate Change Committee, "Net Zero: The UK's contribution to stopping global warming," Committee on Climate Change, 2019.

[4] H. W. K. F. T. U. N. D. &. Z. O. Masaki Yoshio, "Carbon-Coated Si as a Lithium-Ion Battery Anode Material," *Journal of The Electrochemical Society,* vol. 149 , pp. A1598-A1603, 2002.

[5] D. D. ,. a. P. H. L. N. Loïc Baggetto, "Honeycomb-Structured Silicon: Remarkable Morphological," *Advanced Materials,* vol. 23, no. 13, pp. 1563-1566, 2011.

[6] A. M. A. F. W. M. V.O. Shtegman, "ON BUCKLING INDUCED BY A CHEMICAL REACTION," *Materials Physics and Mechanics,* vol. 47, pp. 40-51, 2020.

[7] National Academy of Engineering, "The Draper Prize - Mr Yoshio Nishi," National Academy of Engineering, 2014. [Online]. Available: https://www.nae.edu/105800/Yoshio-Nishi. [Accessed 2022].

[8] S. K. H. L. S. S. Y. Q. Aiping Wang, "Review on modeling of the anode solid electrolyte interphase," *npj Computational Materials,* vol. 4, no. 15, 2018.

[9] W. X. D. W. C. W. W. Jie Xiao, "Stabilization of Silicon Anode for Li-Ion Batteries," *Journal of The Electrochemical Society,* vol. 157, no. 10, pp. A1047-A1051, 2010.

[10] S. N. N. S. O. N. a. Y. A.-L. Chae-Ho Yim, "Towards Improving the Practical Energy Density of Li-Ion," *Journal of The Electrochemical Society,* vol. 164, no. 1, pp. A6294-A6302, 2017.

[11] S. W. L. T. H. B. A. K. W. W. D. N. Y. C. Matthew T. McDowell, "In Situ TEM of Two-Phase Lithiation of Amorphous Silicon," *American Chemical Society,* vol. 13, no. 2, pp. 758-764, 2013.

[12] K. Z. W. Z. S. J. J. V. Matt Pharr, "Kinetics of Initial Lithiation of Crystalline Silicon Electrodes of," *American Chemical Society,* vol. 7, p. 749–756, 2012.

[13] L. Z. S. H. S. X. M. T. Z. a. J. Y. H. Xiao Hua Liu, "Size-Dependent Fracture of Silicon," *ACS Nano,* vol. 6, no. 2, p. 1522–1531, 2012.

[14] I. R. W. L. W. D. N. C. Matthew T. McDowell, "Studying the Kinetics of Crystalline Silicon Nanoparticle Lithiation with In Situ Transmission Electron Microscopy," *Advanced material,* vol. 24, no. 45, pp. 6034-6041, 2012.

[15] E. V.Baranchugov, "Amorphous silicon thin films as a high capacity anodes for Li-ion batteries in ionic liquid electrolytes," *Electrochemistry Communications ,* vol. 9, no. 4, pp. 796-800, 2007.

[16] S. S. D. S. H. P. M. K. D. P. N. K. S. M. Siladitya Pal, "Modeling the delamination of amorphous-silicon thin film anode for," *Journal of Power Sources,* vol. 246, pp. 149-159, 2014.

[17] N.-J. H. Kneusels, "Understanding and Preventing the Degradation of Silicon as a Lithium Ion Battery Anode," University of cambridge, 2019.

[18] M. K. D. R. K. T. C. P. T.-M. L. N. K. N. K. Ranganath Teki, "Nanostructured Silicon Anodes for Lithium IonRechargeable Batteries," *Electrodeposition: Small 20/2009,* vol. 5, no. 20, pp. 2236-2242, 2009.

[19] Y. C. M. S. D. R. M. D. D. P. H. N. O. G. Alexander M. Laptev, "Modeling large patterned deflection during lithiation of," *Extreme Mechanics Letters,* vol. 15, pp. 145-150, 2017.

[20] S. A. F. A. M. W. D. M. Morozov A, "Si Nanopowder Based Anode Material for the Lithium Ion Battery Cell," *Key engineering materials,* vol. 822, pp. 230-238, 2019.

[21] L.-Q. Chen, "Chemical potential and Gibbs free energy," *MRS Bulletin,* vol. 44, no. 7, p. 520–523, 2019.

[22] A. M. J. Ś. Jerzy Wyrwał, "On tensorial forms of thermodynamic potentials in mixtures theory," vol. Volume 46, no. 11–12, pp. 2293-2297, 2009.

[23] A. Morozov, "Numerical and analytical studies of kinetics, equilibrium, and stability of the chemical reaction fronts in deformable solids," Berlin, 2021.

[24] A. B. Freidin, "On the Chemical Affinity Tensor for Chemical Reactions in Deformable Materials," *Mechanics of Solid ,* vol. 50, pp. 260-285, 2015.

[25] Y. Haseli, Chapter Ten - Entropy and chemical equilibrium, Academic press, 2020, pp. 149-168.

[26] A. B. F. Ł. F. Michael Poluektov, "Modelling stress-affected chemical reactions in non-linear viscoelastic solids with application to lithiation reaction in spherical Si particles," *International Journal of Engineering Science,* vol. 128, pp. 44-62, 2018.

[27] A. F. Bower, Applied mechanics of solids, CRC Press, 2010.

[28] A. Freidin, E. Vilchevskaya and I. Korolev, "Freidin, A. B., Vilchevskaya, E. N., & Korolev, I. K. (2014). Stress-assist chemical reactions front propagation in deformable solids. International Journal of Engineering Science, 83 , 57–75. doi: 10.1016/j.ijengsci.2014.03.008," *International Journal of Engineering Science,* vol. 83, pp. 57-75, 2014.

[29] A. K. I. A. S. e. a. Freidin, "Chemical affinity tensor and chemical reaction front propagation: theory and FE-simulations," *International Journal of Fracture,* vol. 202, p. 245–259, 2016.

[30] B. L. S. L. J. Kim, "A comparison among Neo-Hookean model, Mooney-Rivlin model, and Ogden model for chloroprene rubber," *Int. J. Precis. Eng. Manuf,* vol. 13, p. 759–764, 2012.

[31] L. B. Freund and S. Suresh, Thin film materials : stress, defect formation, and surface evolution, Cambridge University Press, 2003.

[32] L. A. L. S. W. C. Y. &. N. W. D. Berla, "Mechanical behavior of electrochemically lithiated silicon," *Journal of Power Sources,* vol. 273, p. 41–51, 2015.

[33] J. S. T. M. O. J. D. C. P. J. M. R. S. S. W. C. Custer, "Density of amorphous Si.," *Applied Physics Letters,* vol. 64, p. 437–439, 1994.

[34] W. L. X. G. C.-M. W. S. Z. Hui Yang, "Strong kinetics-stress coupling in lithiation of Si and Ge anodes," *Extreme Mechanics Letters,* vol. 2, pp. 1-6, 2015.